$$\phi_{ij}^{n+1/2} = \begin{cases} \phi_i^n + (\vec{x}_{ij} - \vec{x}_i) \cdot \vec{\nabla} \phi_i^n - \frac{\Delta t}{2} (\vec{v}_i \cdot \vec{\nabla} \phi_i^n) &, \vec{v}_{ij} \cdot \vec{n}_{ij} \ge 0 \\ \phi_j^n + (\vec{x}_{ij} - \vec{x}_j) \cdot \vec{\nabla} \phi_j^n - \frac{\Delta t}{2} (\vec{v}_j \cdot \vec{\nabla} \phi_j^n) &, \vec{v}_{ij} \cdot \vec{n}_{ij} < 0 \end{cases}$$

$$(49)$$

$$\phi_{i}^{n+1/2} = \begin{cases} \phi_{i}^{n} - \frac{\Delta t}{2} \left(\vec{v}_{i} \cdot \vec{\nabla} \phi_{i}^{n} \right) & , \vec{v}_{ij} \cdot \vec{n}_{ij} \geq 0 \\ \phi_{j}^{n} - \frac{\Delta t}{2} \left(\vec{v}_{j} \cdot \vec{\nabla} \phi_{j}^{n} \right) & , \vec{v}_{ij} \cdot \vec{n}_{ij} < 0 \end{cases}$$

$$(50)$$

The concept of finite element method is applied to determine the gradient quantities. The gradient at the center of control volume, $\nabla \phi_i^n$, is determined by the weighted residuals method and is assumed to be linearly distributed over cell Ω_i ,

$$\vec{\nabla} \phi_i^n = \sum_{k=1}^3 N_k (\bar{x}) \vec{\nabla} \phi_k^n$$
 (51)

where $N_k(\bar{x})$ denotes the linear interpolation functions for the triangular cell and k=1, 2, 3 represent the control volume vertices. By applying the standard Galerkin method and the Gauss's theorem to Eq. (51), the gradient quantities at a grid point are obtained as,

$$\vec{\nabla} \phi_{J,i}^{n} = M^{-1} \left[\int_{\partial \Omega_{i}} \vec{n}_{i}(\upsilon) N_{J}(\upsilon) \phi_{i}^{n} d\upsilon - \int_{\Omega_{i}} \frac{\partial N_{J}(\upsilon)}{\partial \vec{x}} \phi_{i}^{n} d\vec{x} \right]$$
 (52)

where M is the lumped mass matrix and $\nabla \phi_{J,i}^n$ are the contributions of the gradient quantities in the control volume Ω_i to the gradient quantities at the grid point J. In order to determine the total gradient quantities at the grid point J, Eq. (52) is applied to all the volumes surrounding it such that,

$$\vec{\nabla} \phi_J^n = \sum_{i=1}^{NV} \vec{\nabla} \phi_{J,i}^n \tag{53}$$

where NV is the number of the surrounding triangular cells. The gradient quantities at the cell faces, $\nabla \phi_{ij}^n$, is then computed by applying the midpoint quadrature integration rule along the edge that connects grid points I and J.

Figure 13 shows the pure-convection problem of a mixing of hot with cold front. The computational domain is $\Omega = (-4,4) \times (-4,4)$ and an initially straight frontal zone is given by,

$$\phi_0\left(\bar{x}\right) = -\tanh\left(\frac{y}{2}\right) \tag{54}$$

the velocity field is defined as,

$$\vec{v} = -\frac{y}{r} \frac{f_t}{f_{\text{max}}} \vec{i} + \frac{x}{r} \frac{f_t}{f_{\text{max}}} \vec{j}$$
 (55)

where $r = \sqrt{x^2 + y^2}$ is the distance from the origin of the coordinate system, $f_{\text{max}} = 0.385$ is the maximum tangential velocity, and $f_t = \frac{\tanh(r)}{\cosh^2(r)}$. The problem is examined until the final time step is equal to 4. The exact solution is

problem is examined until the final time step is equal to 4. The exact solution is shown by the two- and three-dimensional contour plots in Figs. 13(a)-(b).

The computation is initially performed by using an unstructured mesh consisting of 884 uniform triangular cells. The initial and adaptive meshes with their computed solutions are shown by the two- and three-dimensional contour plots in Figs. 14(a)-(d), respectively. The element size used in the initial mesh is 0.4. The maximum and minimum element sizes of the third adaptive mesh are 1.0 and 0.004, respectively. The figures show that spurious oscillations decrease as the meshes are refined. The exact and computed solutions obtained from the third adaptive mesh are found to be good agreement.

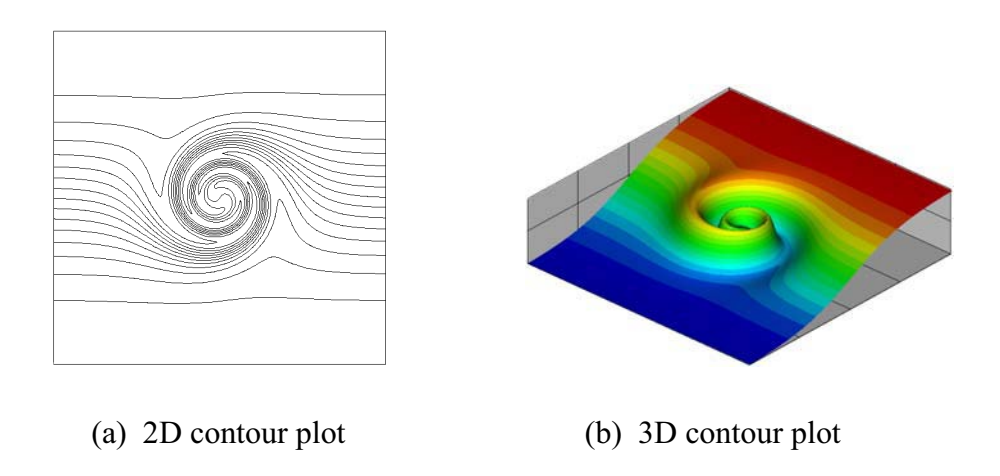
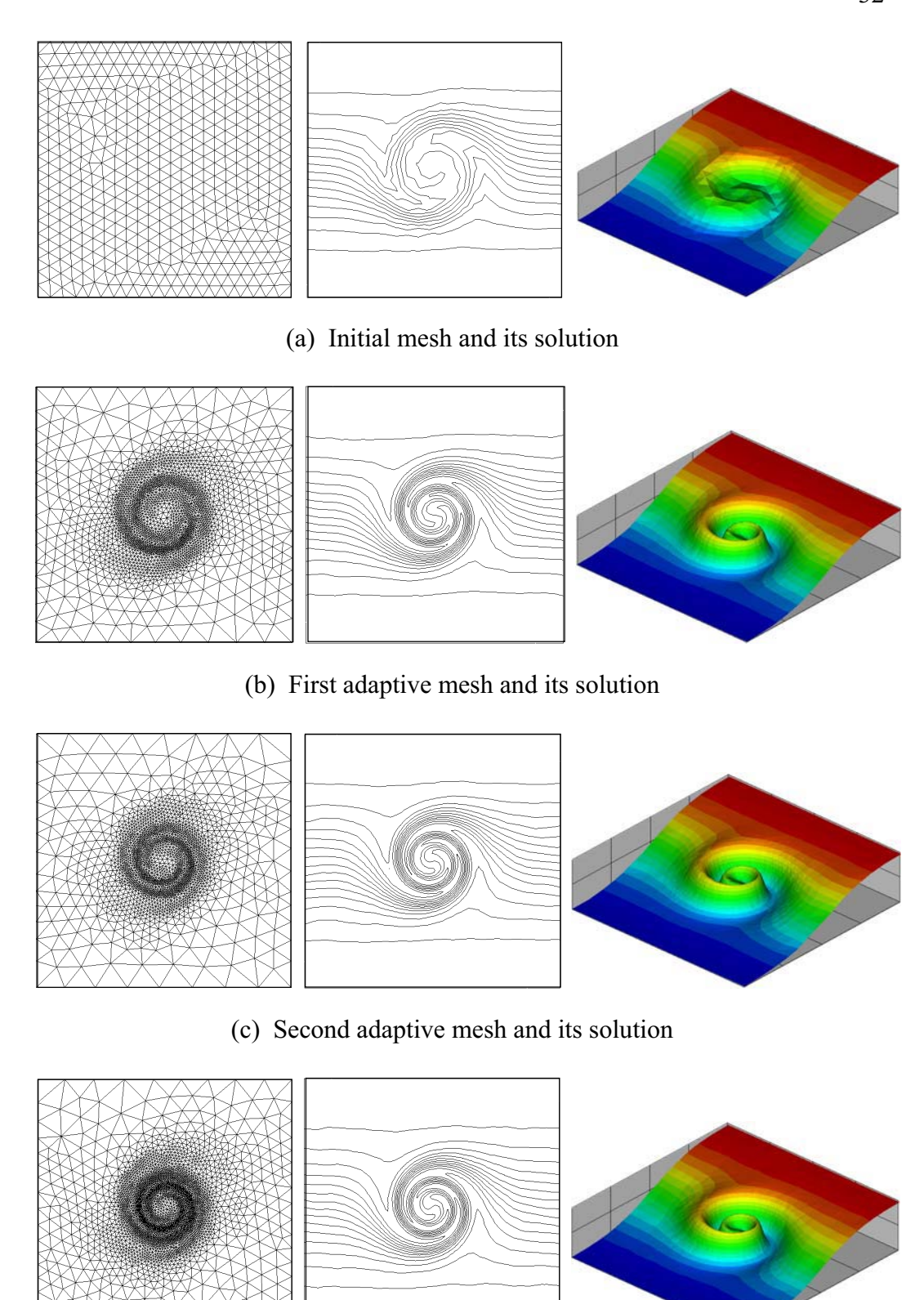


Fig. 13. Exact solution of the mixing of hot with cold front.



(d) Third adaptive mesh and its solution

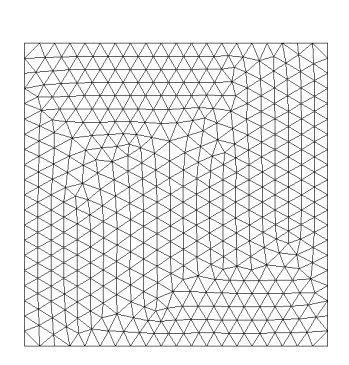
Fig. 14. Adaptive meshes and their computed solutions for the mixing of hot with cold front.

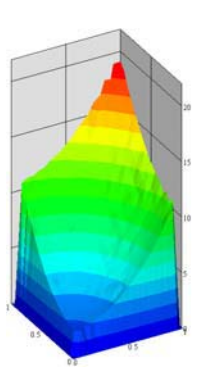
Figure 15 represents a singularly perturbed diffusion-reaction problem. The computational domain is a unit square of $\Omega = (0,1) \times (0,1)$. The initial condition, $\phi_0(\bar{x})$, and the Dirichet boundary condition, $\phi(\bar{x})$, are prescribed as zero. The source term is given by,

$$q = 20(x^2 + y^2) + 4 (56)$$

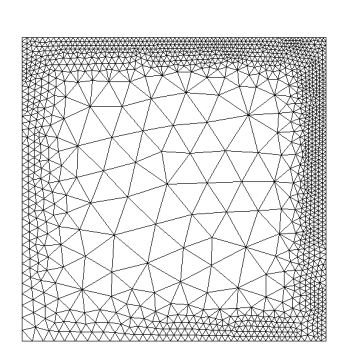
The diffusion coefficient is specified as $\varepsilon = 10^{-3}$, and the reaction coefficient, κ , is set to be 2. This example is performed until the final time step is equal to 5.

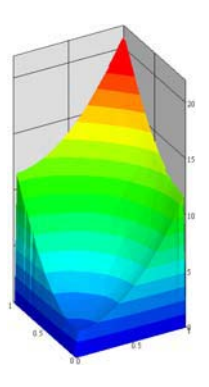
The computation is initially performed by using an unstructured mesh with 884 uniform triangular cells (20 cells along each boundary). As the meshes are adapted with the computed solutions, small element sizes are generated in the region of high solution gradients along the boundary sides x = 1 and y = 1. Figurecs 15(a)-(d) show the initial and adaptive meshes with their corresponding solutions. The computed solution obtained from the initial mesh shows some oscillations without overshooting along the boundary. Oscillations decrease as the meshes are adapted with the solutions.



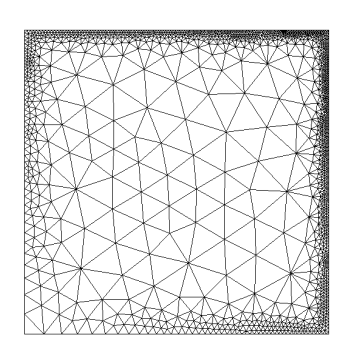


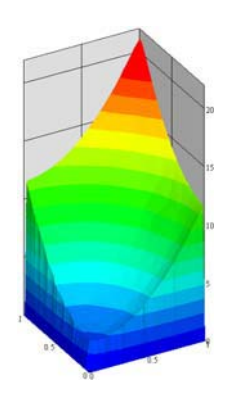
(a) Initial mesh and its solution



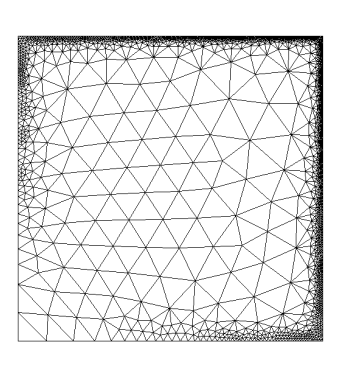


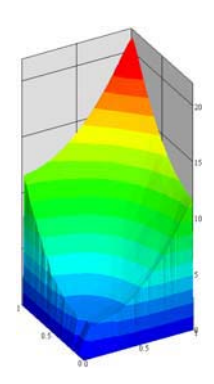
(b) First adaptive mesh and its solution





(c) Second adaptive mesh and its solution





(d) Third adaptive mesh and its solution

Fig. 15. Adaptive meshes and their computed solutions of the corner layer problem.

Low-Speed Incompressible Flow

For low-speed incompressible flow, the Galerkin method with equalorder finite element has been employed. The fundamental laws used to solve twodimensional, steady state, viscous incompressible flow consist of the law of conservation of: (a) mass which is called the continuity equation, and (b) the momentums, and (c) the energy, as follows,

$$\frac{\partial u}{\partial x} + \frac{\partial v}{\partial y} = 0 \tag{57}$$

$$\rho \left[u \frac{\partial u}{\partial x} + v \frac{\partial u}{\partial y} \right] = -\frac{\partial p}{\partial x} + \mu \left[\frac{\partial^2 u}{\partial x^2} + \frac{\partial^2 u}{\partial y^2} \right]$$
 (58a)

$$\rho \left[u \frac{\partial v}{\partial x} + v \frac{\partial v}{\partial y} \right] = -\frac{\partial p}{\partial y} + \mu \left[\frac{\partial^2 v}{\partial x^2} + \frac{\partial^2 v}{\partial y^2} \right]$$
 (58b)

$$\rho \left[u \frac{\partial T}{\partial x} + v \frac{\partial T}{\partial y} \right] = k \left[\frac{\partial^2 T}{\partial x^2} + \frac{\partial^2 T}{\partial y^2} \right]$$
 (58c)

The basic unknowns for the above coupled partial differential equations are the velocity components u and v, the pressure p, and the temperature T.

For the three-node triangular element, the element assumes linear interpolation for both the velocity components and the pressure as,

$$u(x,y) = N_i u_i (59a)$$

$$v(x,y) = N_i v_i (59b)$$

$$p(x,y) = N_i p_i (59c)$$

$$T(x,y) = N_i T_i (59d)$$

where i = 1, 2, 3; and N_i are the element interpolation functions for the velocity, the pressure, and the temperature.

The basic idea of the solution algorithm presented herein is to use the two momentum equations for solving both of the velocity components and use the continuity and the energy equation for solving the pressure and the temperature, respectively. The procedure in deriving the finite element equations corresponding to the momentum and the continuity equations are described as follows.

The two momentum equations (58a-b) are discretized by using the conventional Bubnov-Garlerkin's method. However, a special treatment for the convection terms is incorporated. These terms are approximated by a monotone streamline upwinding formulation to be using with the triangular element. In this approach, the convection terms in the form,

$$u\frac{\partial \phi}{\partial x} + v\frac{\partial \phi}{\partial y} \tag{60}$$

which are related to the transport variable ϕ , are first rewritten in the streamline coordinates as,

$$U_s \frac{\partial \phi}{\partial s} \tag{61}$$

where U_s and $\partial/\partial s$ are the velocity and the gradient along the streamline direction, respectively. For pure convection, the term in Eq. (61) is constant along the streamline. These terms are evaluated by a streamline tracing method which keeps track the direction of the flow within the element.

Using the standard Galerkin approach, each momentum equation is multiplied by weighting function, N_i , and then the diffusion terms are integrated by parts using the Gauss theorem to yield the element equations in the form,

$$[A]\{u\} = \{R_{mx}\} + \{R_{u}\}$$
 (62a)

$$[A]\{v\} = \{R_{nv}\} + \{R_{v}\}$$
 (62b)

where the coefficient matrix [A] contains the known contributions from the convection and diffusion terms. The load vectors on the right-hand side of Eqs. (63a-b) are defined by,

$$\left\{R_{px}\right\} = -\int_{\Omega} \left\{N\right\} \frac{\partial p}{\partial x} d\Omega \tag{64a}$$

$${R_{py}} = -\int_{\Omega} {N} \frac{\partial p}{\partial y} d\Omega$$
 (64b)

$$\{R_u\} = \mu \int_{\Gamma} \{N\} \left[\frac{\partial u}{\partial x} n_x + \frac{\partial u}{\partial y} n_y \right] d\Gamma$$
 (64c)

$$\{R_{\nu}\} = \mu \int_{\Gamma} \{N\} \left[\frac{\partial \nu}{\partial x} n_{x} + \frac{\partial \nu}{\partial y} n_{y} \right] d\Gamma$$
 (64d)

where Ω is the element area and Γ is the surface element boundary. The element equations are assembled to yield the system equations for solving the velocity components. Appropriate boundary conditions are then applied prior to solving such system equations for the updated velocity components.

To derive the discretized pressure equation, the method of weighted residuals is applied to the continuity equation (57),

$$\int_{\Omega} N_{i} \left(\frac{\partial u}{\partial x} + \frac{\partial v}{\partial y} \right) d\Omega = -\int_{\Omega} \left(\frac{\partial N_{i}}{\partial x} u + \frac{\partial N_{i}}{\partial y} v \right) d\Omega + \int_{\Gamma} N_{i} \left(u n_{x} + v n_{y} \right) d\Gamma$$

$$= 0 \tag{65}$$

where the integrations are performed over the element domain Ω and along the element boundary Γ ; n_x and n_y are the direction cosines of the unit vector normal

to element boundary with respect to x and y axis, respectively. As mentioned earlier, the continuity equation is used for solving the pressure, but the pressure term does not appear in the continuity equation. For this reason, the relation between velocities and pressure are thus required. Such relations can be derived from the momentum equations (63a-b) as,

$$A_{ii}u_i = -\sum_{j\neq i} A_{ij}u_j + f_i^u - \int_{\Omega} N_i \frac{\partial p}{\partial x} d\Omega$$
 (66a)

$$A_{ii}v_i = -\sum_{j\neq i} A_{ij}v_j + f_i^v - \int_{\Omega} N_i \frac{\partial p}{\partial y} d\Omega$$
 (66b)

where f_i^u and f_i^v are the surface integral terms as in Eqs. (64c-d). By assuming constant pressure gradient on an element, then,

$$u_i = \hat{u}_i - K_{pi} \frac{\partial p}{\partial x} \tag{67a}$$

$$v_i = \hat{v}_i - K_{pi} \frac{\partial p}{\partial v} \tag{67b}$$

where

$$\hat{u}_i = \frac{-\sum_{j \neq i} A_{ij} u_j + f_i^u}{A_{ii}}$$
(68a)

$$\hat{v}_i = \frac{-\sum_{j \neq i} A_{ij} v_j + f_i^{\nu}}{A_{ii}}$$
 (68b)

$$K_{pi} = \frac{\int_{\Omega} N_i d\Omega}{A_{ii}}$$
 (68c)

By applying the element velocity interpolation functions, Eqs. (59a-b) into the continuity equation (65),

$$-\int_{\Omega} \frac{\partial N_{i}}{\partial x} (N_{j} u_{j}) d\Omega - \int_{\Omega} \frac{\partial N_{i}}{\partial y} (N_{j} v_{j}) d\Omega + \int_{\Gamma} N_{i} (u n_{x} + v n_{y}) d\Gamma = 0$$
 (69)

and introducing the nodal velocities u_j and v_j from Eqs. (67a-b), Eq. (69) becomes,

$$\int\limits_{\Omega} \frac{\partial N_{i}}{\partial x} \Big(N_{j} K_{pj} \Big) \frac{\partial p}{\partial x} d\Omega + \int\limits_{\Omega} \frac{\partial N_{i}}{\partial y} \Big(N_{j} K_{pj} \Big) \frac{\partial p}{\partial y} d\Omega$$

$$= \int_{\Omega} \frac{\partial N_i}{\partial x} (N_j \hat{u}_j) d\Omega + \int_{\Omega} \frac{\partial N_i}{\partial y} (N_j \hat{v}_j) d\Omega - \int_{\Gamma} N_i (u n_x + v n_y) d\Gamma$$
 (70)

Finally, applying the element pressure interpolation functions, Eq. (60c), the above element equations can be written in matrix form with unknowns of the nodal pressures as,

$$[K_x + K_y] \{p\} = \{R_u\} + \{R_y\} + \{R_b\}$$
(71)

where

$$[K_x] = \int_{\Omega} \left\{ \frac{\partial N}{\partial x} \right\} (N_i K_{pi}) \frac{\partial N}{\partial x} d\Omega$$
 (72a)

$$[K_{y}] = \int_{\Omega} \left\{ \frac{\partial N}{\partial y} \right\} (N_{i} K_{pi}) \frac{\partial N}{\partial y} d\Omega$$
 (72b)

$$\{R_u\} = \int_{\Omega} \left(N_j \hat{u}_j\right) \left\{\frac{\partial N_i}{\partial x}\right\} d\Omega$$
 (72c)

$$\{R_{\nu}\} = \int_{\Omega} \left(N_{j}\hat{v}_{j}\right) \left\{\frac{\partial N_{i}}{\partial y}\right\} d\Omega$$
 (72d)

$$\{R_b\} = -\int_{\Gamma} \{N\} \left(u n_x + v n_y \right) d\Gamma \tag{72e}$$

The above element pressure equations are assembled to form the global equations, nodal boundary conditions for pressure are imposed prior to solving for the updated nodal pressures. The finite element equations corresponding to the energy equation can be derived in the same fashion. Typical solutions obtained from the above formulation include the lid-driven cavity flow as shown in Figs. 16-18. The adaptive meshing technique has also been implemented with the formulation as demonstrated by the flow past a cylinder in Figs. 19-20.

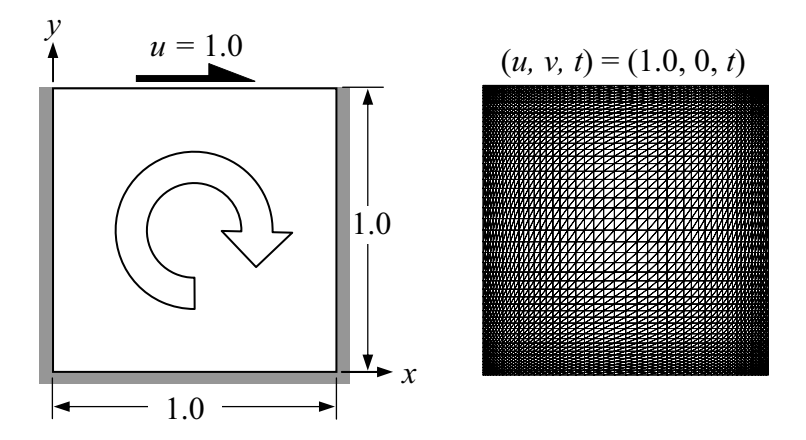


Fig. 16. Problem statement and finite element model of the lid-driven cavity flow problem.

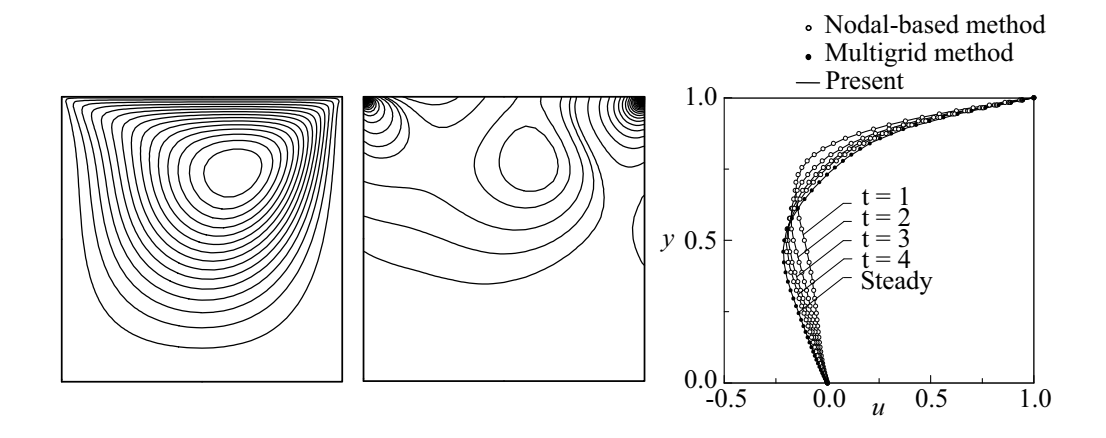
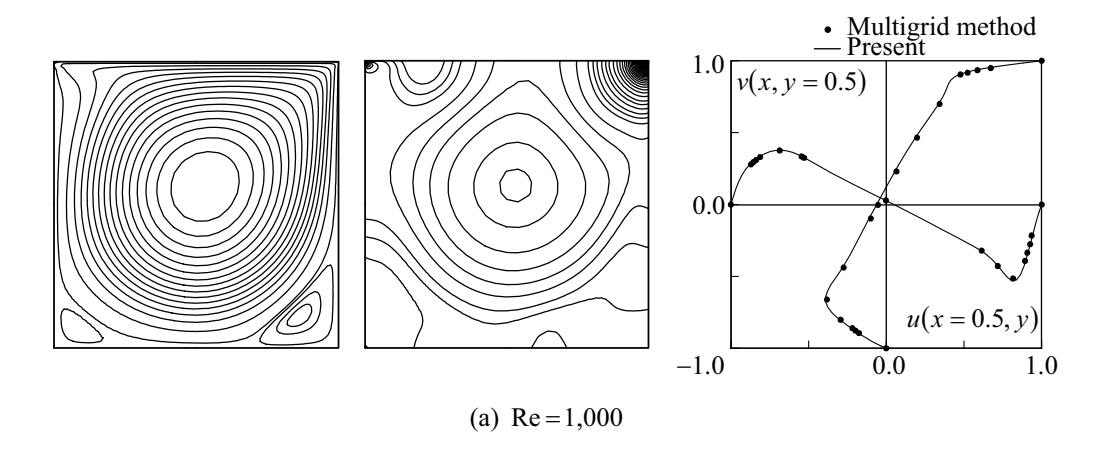


Fig. 17. Predicted streamline, pressure contours and velocity profile of *x*-direction on x = 0.5 at Re = 100



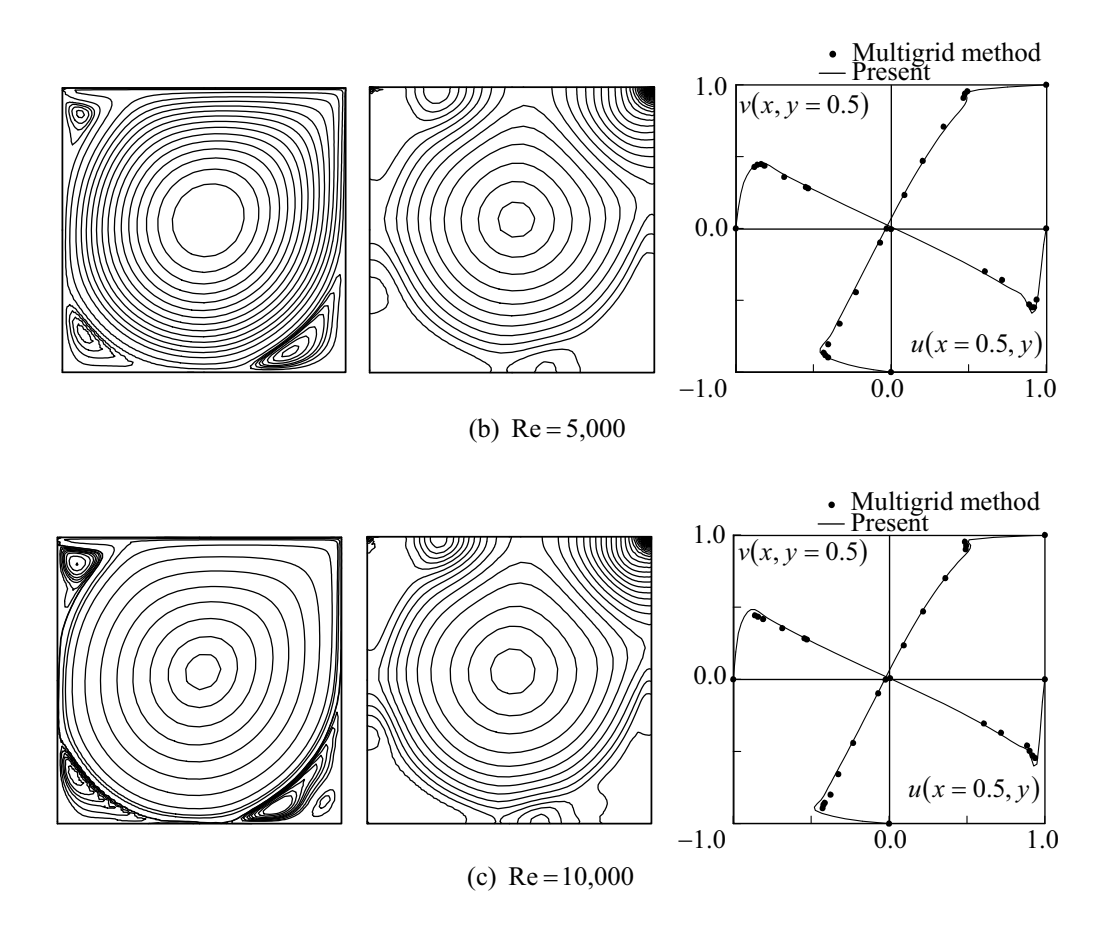


Fig. 18. Predicted streamline, pressure contours and velocity profiles in the x and y directions at Re = 1,000, 5,000 and 10,000.

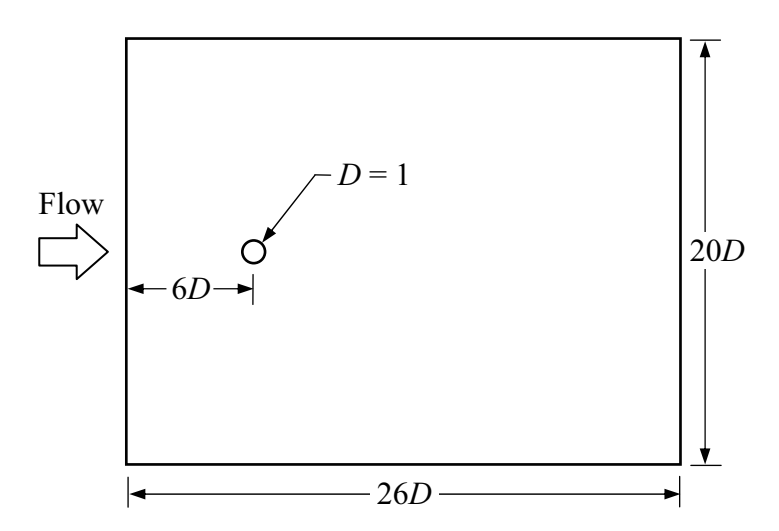


Fig. 19. Problem statement of the flow past a cylinder.

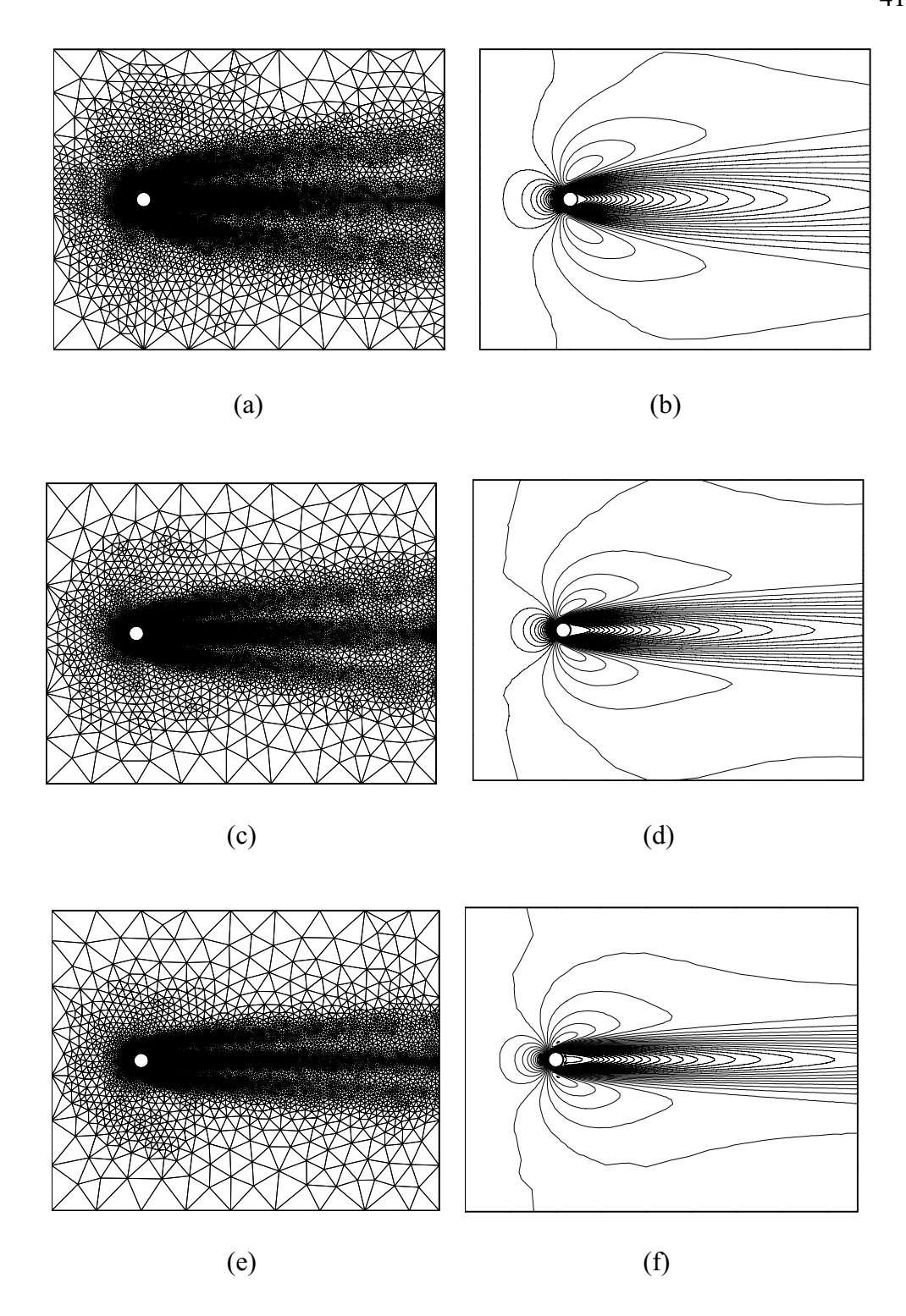


Fig. 20. Adaptive meshes and corresponding velocity contours: (a)-(b) Re = 10; (c)-(d) Re = 20; and (e)-(f) Re = 30.

Figure 21 shows the problem statement of the thermally driven flow in concentric cylinders. The fluid is freely convected in the annular space between long, horizontal concentric cylinders due to high temperature on the inner cylinder

and lower temperature on the outer cylinder. This problem was studied experimentally by Kuehn and Goldstein for which their results can be used for comparison. All results are at the Prandtl number of 0.7 with a ratio of gap width to inner-cylinder diameter (L/D) of 0.8. The finite element model consisting of 2,170 nodes and 4,200 elements are shown in Fig. 21. Figure 22 presents the predicted temperature contours on the left half and the velocity vectors on the right half at the Rayleigh numbers of 3,000 and 10,000. Figure 23 shows the comparisons of the equivalent conductivities at the inner and outer cylinder surfaces. The figures show good agreement of the predicted solutions and the experimental results.

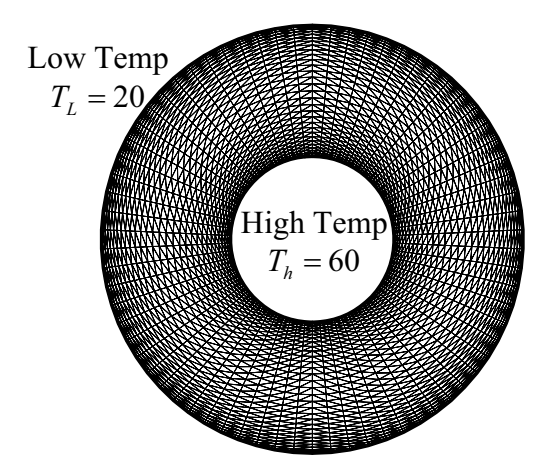


Fig. 21. Finite element model for thermally driven flow in concentric cylinders.

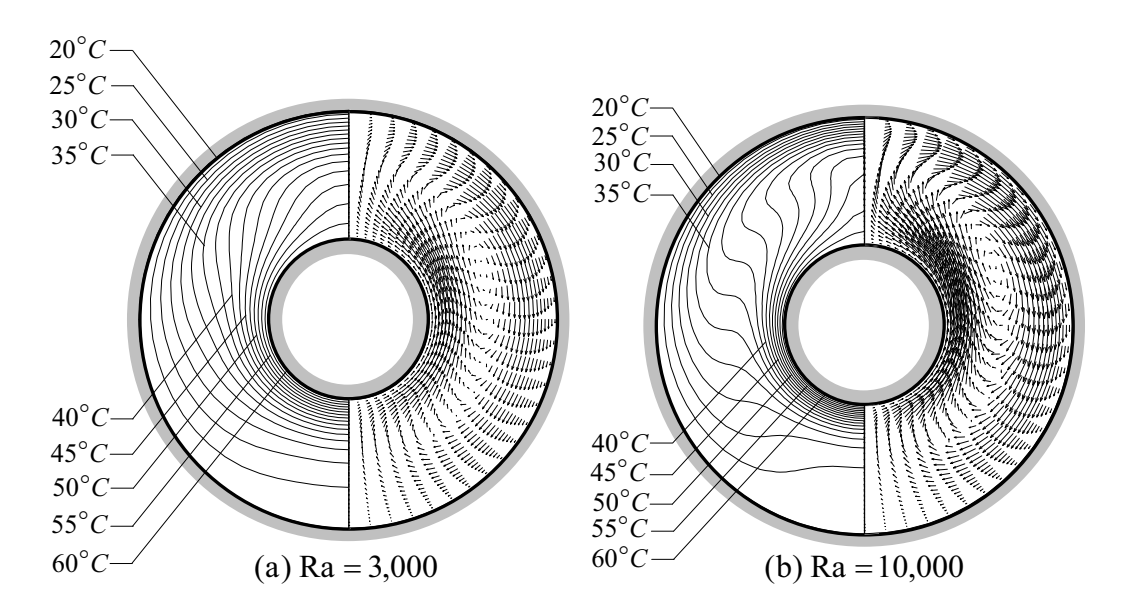


Fig. 22. Predicted temperature contours and velocity vectors at Rayleigh numbers of 3,000 and 10,000.

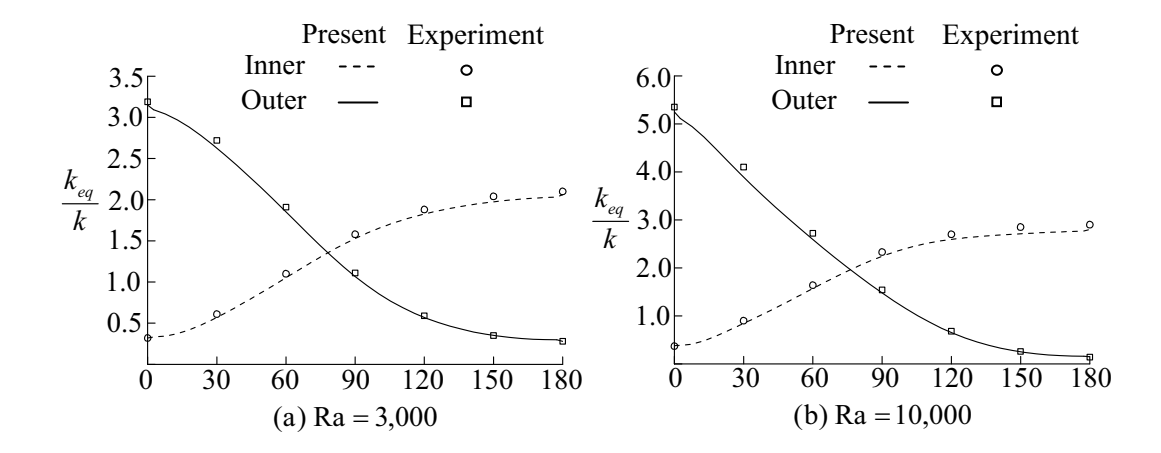


Fig. 23. Comparison of the local equivalent conductivities at Rayleigh numbers of 3,000 and 10,000.

Heat Transfer in Solids

For two-dimensional domain Ω bounded by surface S in the x-y coordinate system, the Poisson's equation can be written in the conservation form as,

$$\frac{\partial E}{\partial x} + \frac{\partial F}{\partial y} = f(x, y) \tag{73}$$

where f(x,y) denotes the source function. The flux components E and F are defined by,

$$E = -c\frac{\partial U}{\partial x}$$
 and $F = -c\frac{\partial U}{\partial y}$ (74)

where U is the primary variable and c is the material property that depends on types of problem. For examples, c may represent the thermal conductivity and the permeability coefficient for the heat transfer and the magnetostatics problem, respectively. The Poisson's equation shown in Eq. (73) is to be solved together with appropriate boundary conditions that may consist of,

$$U_1(x,y) \quad \text{on } S_1 \tag{75a}$$

$$c\frac{\partial U}{\partial n} + d(U - U_{\infty}) = q \quad \text{on } S_2$$
 (75b)

where d and $\,U_{\scriptscriptstyle \infty}\,$ are constants and q is the secondary variable.

Nodeless Variable Flux-Based Finite Element Formulation

The flux-based formulation is implemented herein to derive the finite element equations associated with the nodeless variable element. For the triangular nodeless variable element, the distribution of the primary variable over the element is assumed in the form,

$$U(x,y) = \sum_{i=1}^{6} N_i(x,y)U_i = \lfloor N(x,y) \rfloor \{U\}$$
 (76)

where $\lfloor N(x,y) \rfloor$ consists of the element interpolation functions, and $\{U\}$ is the vector of the unknown primary variables and the nodeless variables. The nodal primary variables are U_1 through U_3 , while U_4 through U_6 are the nodeless variables. The element interpolation functions, N_1 , N_2 , N_3 are identical to the element interpolation functions L_1 , L_2 , L_3 used for the standard three-node triangular element. The nodeless variable interpolation functions implemented in this paper are,

$$N_4 = L_2 L_3$$
 ; $N_5 = L_1 L_3$; $N_6 = L_1 L_2$ (77)

Each nodeless variable interpolation function varies quadratically along one edge and vanishes along the other edges. To derive the finite element matrices by means of the flux-based formulation, the method of weighted residuals is first applied to Eq. (73),

$$\int_{\Omega} N_i \left(\frac{\partial E}{\partial x} + \frac{\partial F}{\partial y} - f(x, y) \right) d\Omega = 0$$
 (78)

where Ω is the element domain. The Gauss's theorem is then applied to the flux derivative terms to yield,

$$\int_{\Omega} N_i \frac{\partial E}{\partial x} d\Omega = \int_{S} N_i E n_x d\Gamma - \int_{\Omega} \frac{\partial N_i}{\partial x} E d\Omega$$
 (79a)

$$\int_{\Omega} N_{i} \frac{\partial F}{\partial y} d\Omega = \int_{S} N_{i} F n_{y} d\Gamma - \int_{\Omega} \frac{\partial N_{i}}{\partial y} F d\Omega$$
 (79b)

where S is the element boundary. By substituting Eqs. 79(a)-(b) into Eq. (78) to yield,

$$\int_{\Omega} \frac{\partial N_i}{\partial x} E d\Omega + \int_{\Omega} \frac{\partial N_i}{\partial y} F d\Omega = \int_{S} N_i E n_x d\Gamma + \int_{S} N_i F n_y d\Gamma - \int_{\Omega} N_i f(x, y) d\Omega$$
 (80)

In the flux-based formulation, the element flux distributions are computed from the actual nodal fluxes as,

$$E = \sum_{i=1}^{3} \overline{N_i} E_i = \left\lfloor \overline{N} \right\rfloor \{E\} \quad \text{and} \quad F = \sum_{i=1}^{3} \overline{N_i} F_i = \left\lfloor \overline{N} \right\rfloor \{F\}$$
 (81)

where $\lfloor \overline{N} \rfloor$ are the standard linear element interpolation functions, i.e., $\lfloor L_1 \ L_2 \ L_3 \rfloor$. The $\{E\}$ and $\{F\}$ are the vectors of the actual nodal fluxes,

$$\{E\} = \begin{cases} -c \left\lfloor \frac{\partial N}{\partial x} \right\rfloor \{U\} \right|_{1} \\ -c \left\lfloor \frac{\partial N}{\partial x} \right\rfloor \{U\} \right|_{2} \\ -c \left\lfloor \frac{\partial N}{\partial x} \right\rfloor \{U\} \right|_{3} \end{cases} \quad \text{and} \quad \{F\} = \begin{cases} -c \left\lfloor \frac{\partial N}{\partial y} \right\rfloor \{U\} \right|_{1} \\ -c \left\lfloor \frac{\partial N}{\partial y} \right\rfloor \{U\} \right|_{2} \\ -c \left\lfloor \frac{\partial N}{\partial y} \right\rfloor \{U\} \right|_{3} \end{cases}$$
(82)

Determination of nodal fluxes depends on the types of problem considered. For heat transfer problem, as an example, the nodal heat fluxes are related to the temperature gradients through the Fourier's law given by,

$$\{E\} = q_{x} = \begin{cases} -k \left\lfloor \frac{\partial N}{\partial x} \right\rfloor \{T\} \right|_{1} \\ -k \left\lfloor \frac{\partial N}{\partial x} \right\rfloor \{T\} \right|_{2} \end{cases} \quad \text{and} \quad \{F\} = q_{y} = \begin{cases} -k \left\lfloor \frac{\partial N}{\partial y} \right\rfloor \{T\} \right|_{1} \\ -k \left\lfloor \frac{\partial N}{\partial y} \right\rfloor \{T\} \right|_{2} \end{cases}$$
(83)

By substituting Eq. (83) into Eq. (81), the finite element equations are,

$$[D_x]\{E\} + [D_y]\{F\} = -\{R\} + \{B\}$$
(84)

where the matrices $[D_x]$ and $[D_y]$ in Eq. (84) are,

$$[D_x] = \int_A \left\{ \frac{\partial N}{\partial x} \right\} \left[\overline{N} \right] dA \quad \text{and} \quad [D_y] = \int_A \left\{ \frac{\partial N}{\partial y} \right\} \left[\overline{N} \right] dA \tag{85}$$

and A is the element area. The element nodal vector $\{R\}$ associated with the source variable is,

$$\{R\} = \int_{A} \{N\} f(x, y) \, dA \tag{86}$$

and the vector $\{B\}$ representing the boundary nodal vector is,

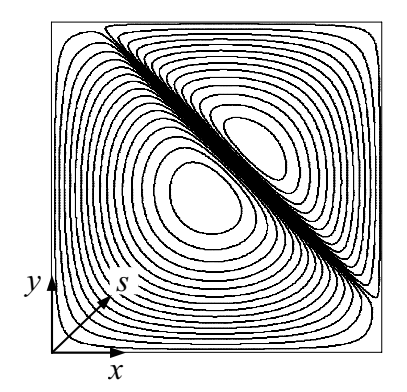
$$\{B\} = \int_{S} \{N\} \left\lfloor \overline{N} \right\rfloor d\Gamma (l\{E\} + m\{F\})$$

$$= \int_{S} \{N\} \left\lfloor \overline{N} \right\rfloor d\Gamma \{q\}$$
(87)

where l and m are the components of the unit vector normal to the element boundary. The vector $\{q\}$ appearing in the above Eq. (87) may be replaced by different types of boundary conditions as shown in Eq. (75b). The interpolation functions in Eq. (87) needed for integration along a typical element side are,

$$N_1 = 1 - \frac{x}{L}$$
 ; $N_2 = \frac{x}{L}$; $N_3 = \frac{x}{L} \left(1 - \frac{x}{L} \right)$ (88)

where L is the length of element edge and x is the local coordinate along the edge. The finite element equations, Eq. (84), are derived for all the elements prior to assembling to yield the system equations. Appropriate boundary conditions of the given problem are then applied. Finally, the system equations are iteratively solved for the nodal solutions and the nodeless variables using the preconditioned conjugate gradients method with an element-by-element approximation technique. Figures 24-26 show the application of the nodeless variable finite element and the use of an adaptive meshing technique for analyzing the temperature distribution in a plate subjected to complex surface heating.



$$\nabla^2 U = -Q(x, y)$$
 in Ω
for $0 \le x \le 1$; $0 \le y \le 1$
with $U = 0$ along edges.

Fig. 24. Governing equation, boundary conditions and solution contours for problem with high solution gradient in a square region.

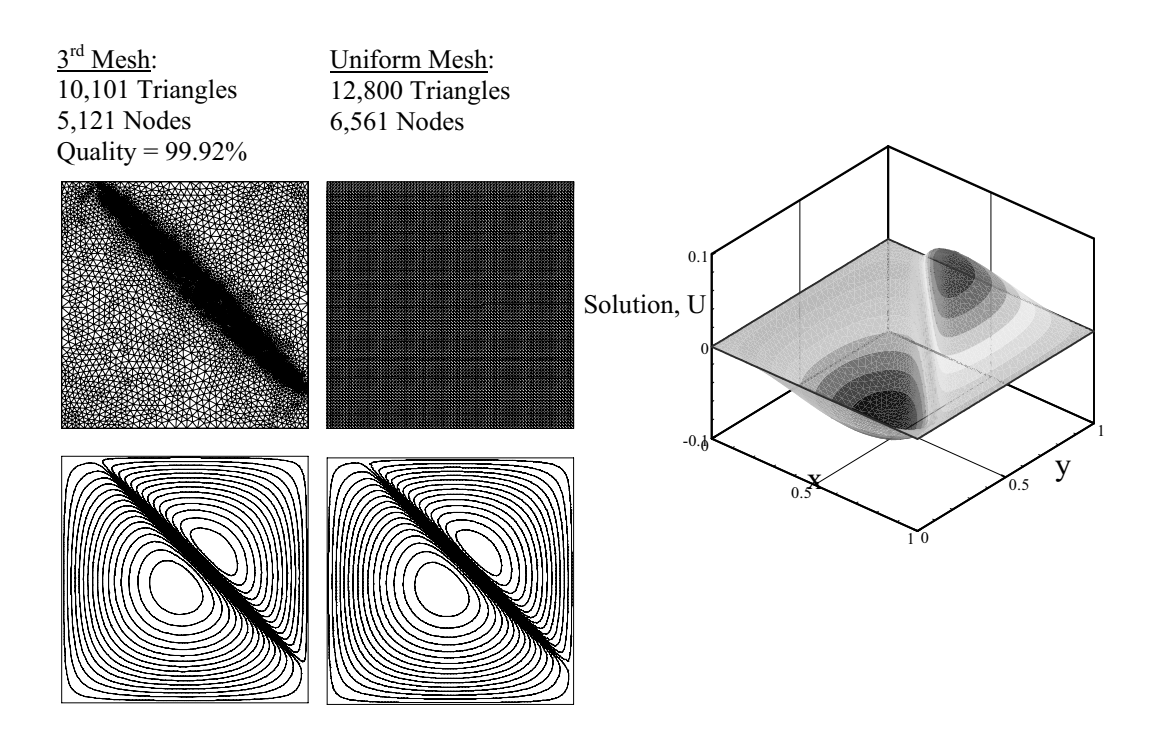


Fig. 25. Uniform and adaptive meshes with their solution contours for the problem with high solution gradient.

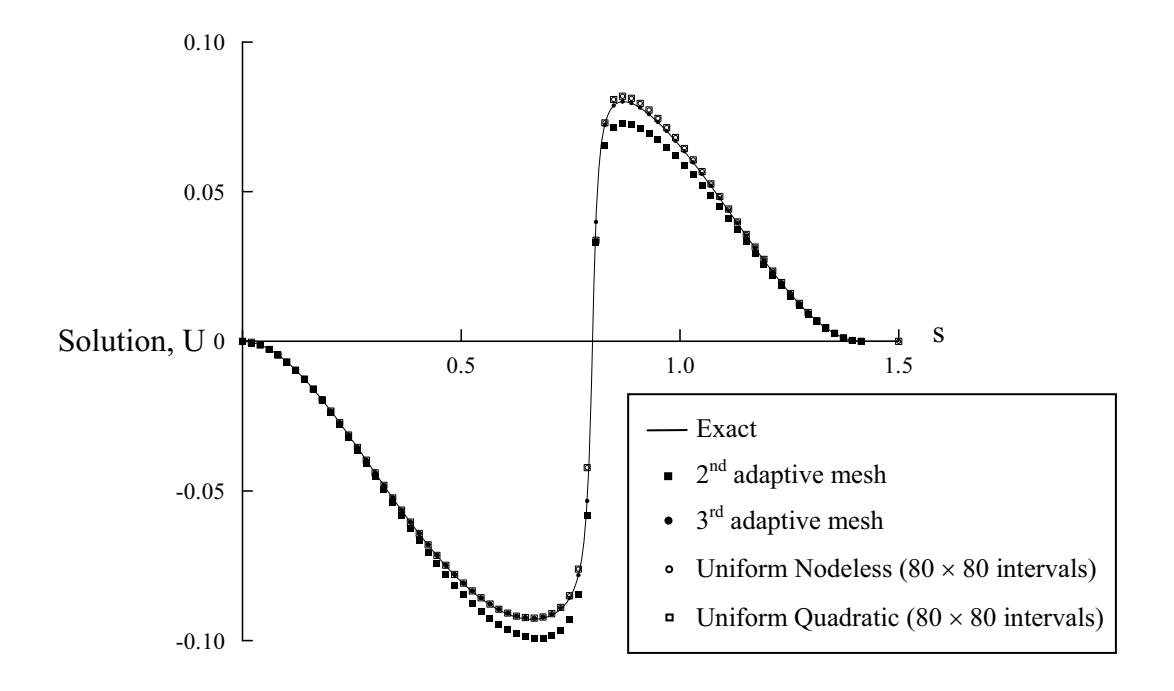


Fig. 26. Comparison of the exact and predicted solutions for the problem with high solution gradient.

The finite element formulation above has been extended for the thermal analysis of convectively-cooled solids. The equations which govern convectively-cooled solids are the one-dimensional conservation of energy for the fluid flow and the two-dimensional conservation of energy equation for the solid. The energy equation for the fluid flow is given by

$$\rho_f c_f u_f A_f \frac{\partial T_f}{\partial x} - k_f A_f \frac{\partial^2 T_f}{\partial x^2} - hp \left(T_f - T_s \right) - Q_f A_f = 0$$
 (89)

and the energy equation in the solid is,

$$k_{s} \left(\frac{\partial^{2} T_{s}}{\partial x^{2}} + \frac{\partial^{2} T_{s}}{\partial y^{2}} \right) - Q_{s} = 0$$
 (90)

where subscript f and s are the fluid and solid, respectively; u is the velocity in x direction, ρ is the density, c is the specific heat, k is the coefficient of thermal conductivity, k is the convective heat transfer coefficient, k is the perimeter, k is the internal heat generation rate per volume and k is the temperature.

Nodeless variable finite element equations can be derived from the method of weighted residuals. The mass transport element and triangular element are used in the derivation. For both elements, distributions of the temperature over the elements are assumed in the form

$$T(x) = \sum_{i=1}^{3} N_i(x) T_i$$
 (91)

$$T(x,y) = \sum_{i=1}^{6} N_i(x,y) T_i$$
 (92)

where N_i consists of the element interpolation functions and T_i are the vector of the unknown temperatures and the nodeless variables. Equations (91) and (92) include the nodeless variable interpolation functions in fluid and solid respectively. For the fluid, the nodal temperatures are T_1 and T_2 , while T_3 is the nodeless variable. For the solid, the nodal temperatures are T_1 through T_3 , while T_4 through T_6 are the nodeless variables. The element interpolation functions, N_1 and N_2 in fluid, N_1 through N_3 in solid are for the standard two-node line and three-node triangular element, respectively. The nodeless variable interpolation functions used herein are,

For fluid,

$$N_3 = N_1 N_2 \tag{93}$$

For solid,

$$N_4 = 4L_2L_3$$

$$N_5 = 4L_1L_3$$

$$N_6 = 4L_1L_2$$
(94)

To derive the nodeless variable finite element matrices, the method of weighted residuals is first applied to Eq. (89) and Eq. (90). Integration by parts is then performed by using the Gauss theorem to yield the boundary term for applying various types of boundary conditions. The nodeless variable finite element equations are,

For fluid,

$$\int_{0}^{L} kA \left\{ \frac{\partial N}{\partial x} \right\} \left[\frac{\partial N}{\partial x} \right] dx \left\{ T_{f} \right\} + \int_{0}^{L} mc \left\{ N \right\} \left[\frac{\partial N}{\partial x} \right] dx \left\{ T_{f} \right\} + \int_{0}^{L} hp \left\{ N \right\} \left[N \right] dx \left\{ T_{f} \right\}
- \int_{0}^{L} hp \left\{ N \right\} \left[N \right] dA \left\{ T_{s} \right\} = \left(\left\{ N \right\} kA \frac{\partial T_{f}}{\partial x} \right) \Big|_{0}^{L} + \int_{0}^{L} QA \left\{ N \right\} dx$$
(95)

For solid,

$$\int_{A} kt \left\{ \left\{ \frac{\partial N}{\partial x} \right\} \left\lfloor \frac{\partial N}{\partial x} \right\rfloor + \left\{ \frac{\partial N}{\partial y} \right\} \left\lfloor \frac{\partial N}{\partial y} \right\rfloor \right\} dA \left\{ T_{s} \right\}$$

$$= \int_{\Gamma} k \left\{ N \right\} t \left(\frac{\partial T_{s}}{\partial x} n_{x} + \frac{\partial T_{s}}{\partial y} n_{y} \right) d\Gamma + \int_{A} \left\{ N \right\} Qt dA \tag{96}$$

where A is the element area, \dot{m} is the mass flow rate, L is the element length, Γ is the element boundary, t is the element thickness, n_x and n_y are the direction cosines of the unit vector normal to the edge. The above equations can be written in matrix form as shown below.

For fluid,

$$\left(\left[K_{c}\right]+\left[K_{v}\right]+\left\lceil K_{f-s}\right\rceil\right)\left\{T_{f}\right\}-\left\lceil K_{f-s}\right\rceil\left\{T_{s}\right\} = \left\{Q_{Q}\right\} \tag{97}$$

For solid,

$$\left(\left[K_{c}\right]+\left[K_{f-s}\right]\right)\left\{T_{s}\right\}-\left[K_{f-s}\right]\left\{T_{f}\right\} = \left\{Q_{O}\right\} \tag{98}$$

These finite element equations can be written together as

$$\begin{bmatrix}
[K_c] + [K_v] + [K_{f-s}] & -[K_{f-s}] \\
-[K_{f-s}] & [K_c] + [K_{f-s}]
\end{bmatrix}
\begin{bmatrix}
T_f \\
T_s
\end{bmatrix} =
\begin{bmatrix}
Q_{Q_f} \\
Q_{Q_s}
\end{bmatrix}$$
(99)

where $\left[K_{c}\right]$ is the conduction matrix, $\left[K_{v}\right]$ is the mass transport convection matrix, $\left[K_{f-s}\right]$ is the convection matrix between the fluid and solid, $\left\{Q_{Q}\right\}$ is the internal heat generate load vector, $\left\{T_{f}\right\}$ and $\left\{T_{s}\right\}$ are the vectors of nodal temperatures in fluid and solid, respectively.

The first example for evaluation the nodeless finite element formulation is the problem of convectively-cooled solid subjected to uniform heating as shown in Fig. 27. In the figure, the upper wall is subjected to uniform heating q. Heat is transferred to the lower wall by the internal fluid flow. The other walls of the problem are assumed to be adiabatic.

The parameters employed in the computation are as follows: the dimension H = 0.1 m and L = 2 m, the uniform heating parameter q = 8,000 W/m², the thermal conductivity $k_s = 1,000$ W/m-K, the flow channel parameters are Pe = 200 (Re = 286) and Pe = 400 (Re = 572) with Pr = 0.7. The finite element model, consisting of 408 nodes and 650 elements as shown in Fig. 28, is used in the analysis.

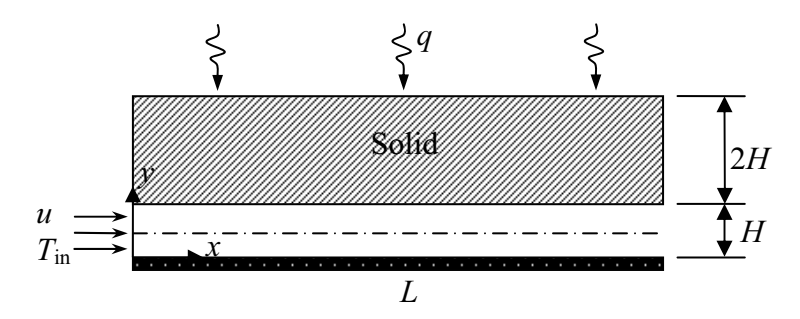


Fig. 27. Problem statement of convectively-cooled solid subjected to uniform heating.

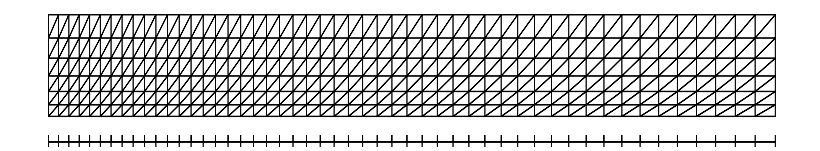
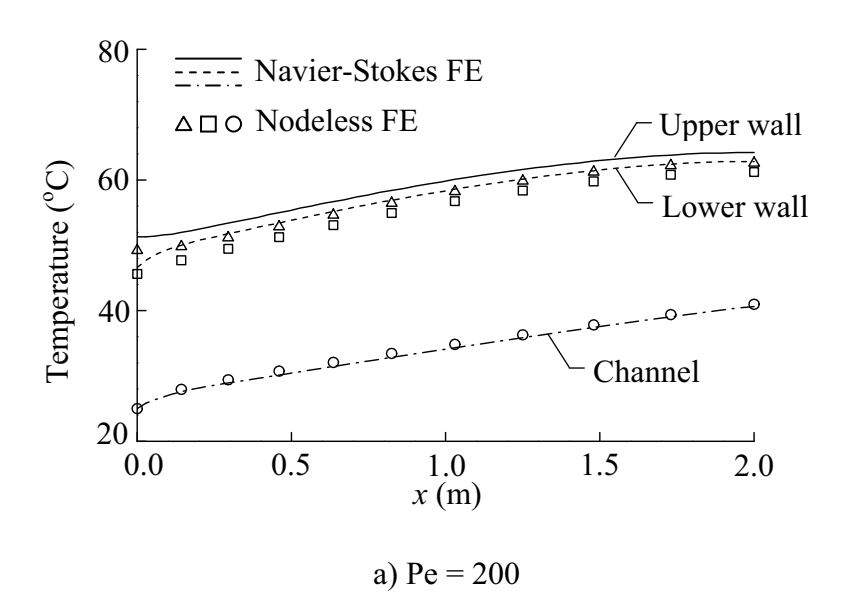


Fig. 28. Nodeless variable finite element model consisting of 650 triangles and 408 nodes.

Figure 29 shows the predicted temperature distributions along the upper wall, the lower wall and along the channel. The predicted temperature distribution in solid is shown in Fig. 30. Figure 31 shows the predicted temperature distributions at x = L, Pe=200 at different conductivity ratios, $K=k_s/k_f$. The solutions are compared with the results obtained from the Navier-Stokes finite element method. The figure shows good agreement of the solutions.



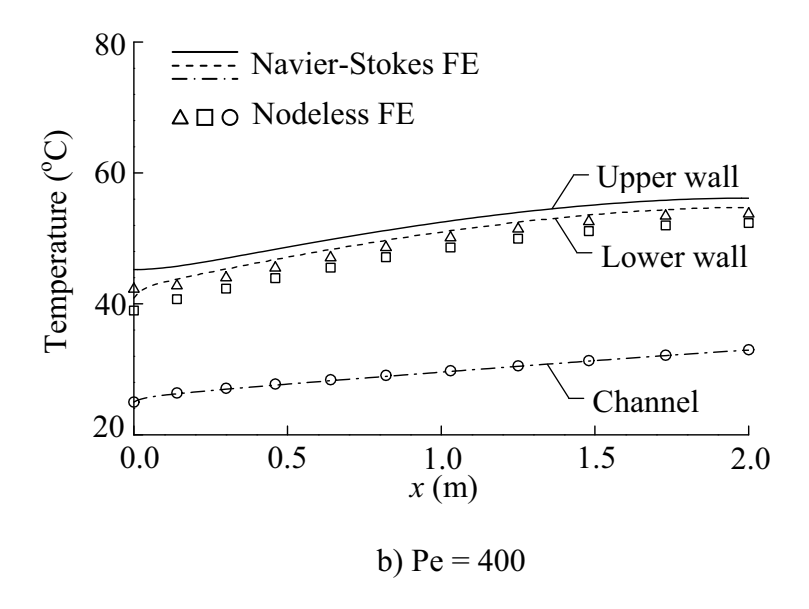


Fig. 29. Comparison of Navier-Stokes and the nodeless variable finite element calculated the predicted temperature distributions along the two walls and the channel at Pe = 200 and Pe = 100.

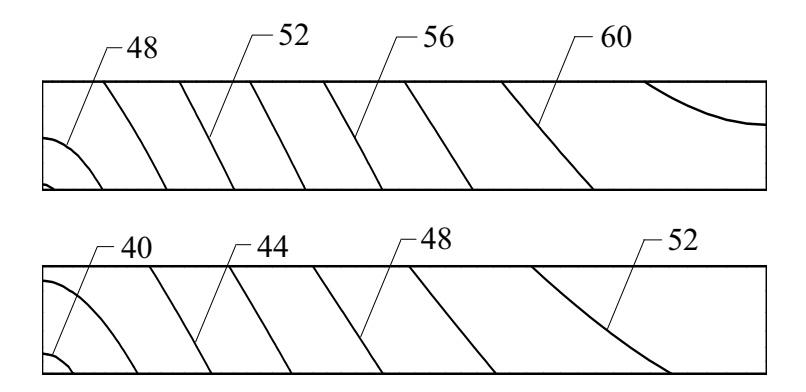


Fig. 30. Predicted temperature contours for convectively-cooled solid subjected to uniform heating at Pe = 200 and Pe = 400.

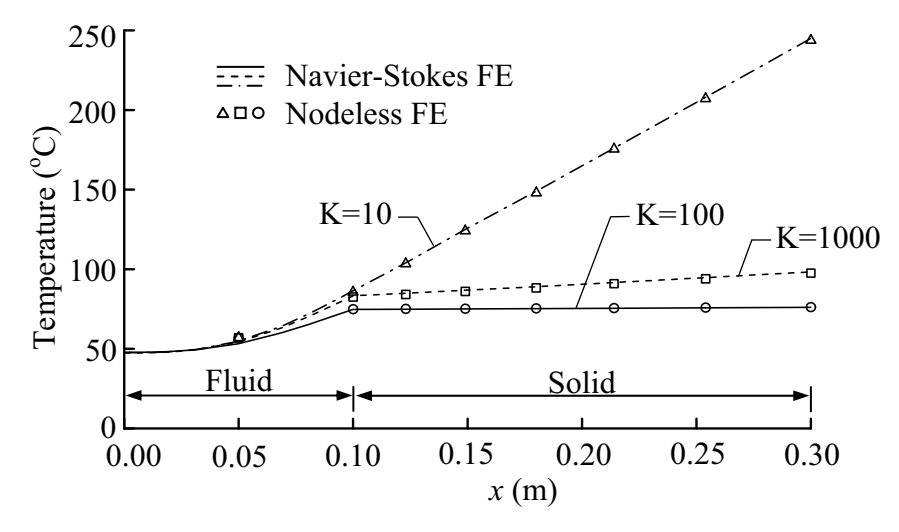


Fig. 31. Comparison of the predicted temperatures from the Navier-Stokes and the nodeless variable finite element methods at x = L and Pe = 200.

To further evaluate the performance of the nodeless variable finite element method incorporated with the adaptive meshing technique, a plate subjected to an intense heating is considered. The intense heating is simulated as a square width. The analysis is performed by using two cases. In the first case, three edges of plate are fixed at zero temperature. In the second case, the plate has heat transfer by fluid flow along the lower edge. The inlet temperature is specified as zero while all other edges are insulated.

In the first case as shown in Fig. 32, the exact plate temperature response can be derived in the form

$$T(\xi, y) = \frac{q}{Lk} \left\{ \sum_{n=2,4}^{\infty} \frac{1}{\lambda_n^3} \left[\sin\left(\frac{n\pi\xi}{2L}\right) \frac{\sinh(\lambda_n y)}{\cosh(\lambda_n H)} \right] + \sum_{n=1,3}^{\infty} \frac{1}{\lambda_n^3} \left[\frac{n\pi}{L} \sin(\alpha) \right] \right\}$$

$$\left[\cos\left(\frac{n\pi\xi}{2L}\right)\frac{\sinh(\lambda_n y)}{\cosh(\lambda_n H)}\right]$$
 (100)

where the origin of the ξ - y coordinate system is shown in Fig. 32, q is the heat source, H is the plate width, k is the plate thermal conductivity. The parameter α and λ_n in Eq. (100) are defined by

$$\alpha = \frac{n\pi w}{2L} \tag{101}$$

$$\lambda_n = \sqrt{\frac{n^2 \pi^2}{4L^2}} \tag{102}$$

where L is the plate length and w is the width of the heat source.

Figure 33 shows a structured finite element mesh consisting of 5,600 elements and 3,208 nodes, and an adaptive mesh with only 742 elements and 446 nodes. Table 1 compares the predicted peak temperature obtained from the two finite element meshes using the convectional and nodeless variable finite element methods. The values in the brackets denote the percentage error of the peak temperature as compared to the exact solution. Table 1 indicates that the adaptive mesh uses fewer elements than the structured mesh but can provide higher solution accuracy.

Figure 34 shows the adaptive mesh and the computed temperature contours. Details of the adaptive mesh near the intense heating location and the temperature contours are shown in the lower figures. These figures highlight small clustered elements are generated in the region of steep temperature gradients to capture the peak temperature and localized temperature distribution. At the same time, larger elements are generated in the other regions to reduce the computational time and the computer memory. The comparison of the exact and the predicted temperature distributions along the top edge is shown in Fig. 35. The figure shows that the temperature distribution obtained from the adaptive meshing technique combined with the nodeless variable finite element method is in good agreement with the exact solution.

For the second case as described by Fig. 36, a fluid with fully developed inlet velocity and temperature profiles flows along the lower edge of

plate. The parameters of fluid used in the computation are as follows: the thermal conductivity $k_f = 0.32$ W/m-K, the specific heat $c_f = 1200$ W/m-K, the density $\rho = 54$ kg/m³, the mass flow rate $\dot{m} = 0.054$ kg/s, the convection coefficient h = 929.52 W/m²-k. At the intense heating location, the predicted peak temperature is 218.30 °C obtained from the nodeless variable finite element method while the conventional finite element method yields the temperature of 217.91 °C.

Figure 37 shows the adaptive mesh that consists of 1,096 elements and 667 nodes with its computed temperature solution. Details of the adaptive mesh near the intense heating location and the temperature contours are shown in the lower insert of the figure. Figure 38 shows the computed temperature distributions along the top edge, the lower edge and the fluid temperature in the channel obtained from the adaptive meshing technique combining with the nodeless variable finite element method. The solution obtained is different from the first case because of heat transfer along the lower edge varies with the fluid flow and the wall temperature.

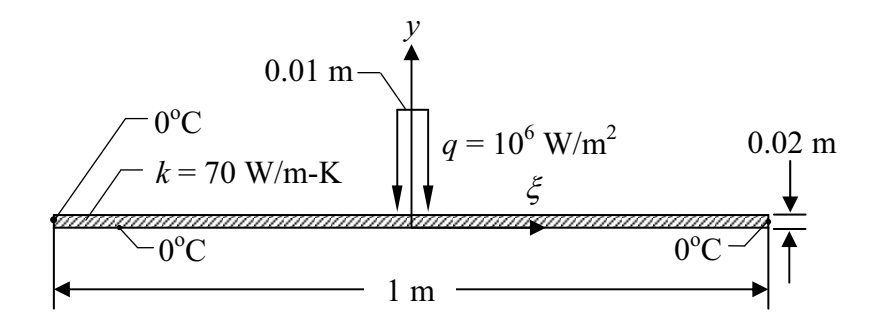


Fig. 32. Problem statement of a plate subjected intense heating.

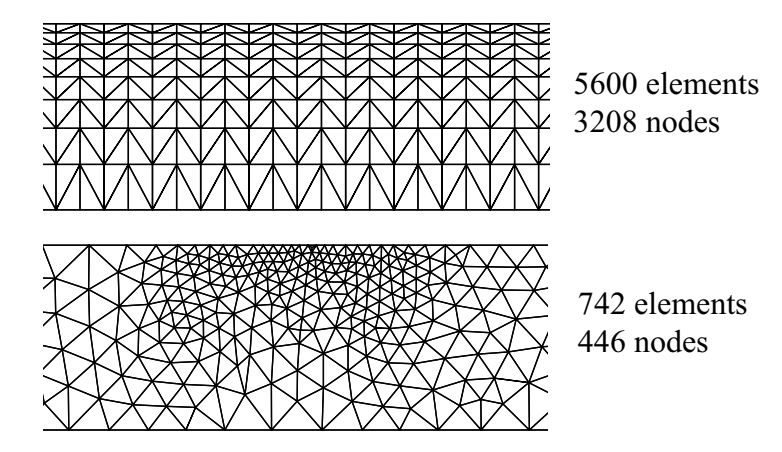


Fig. 33. Structured and adaptive mesh models.

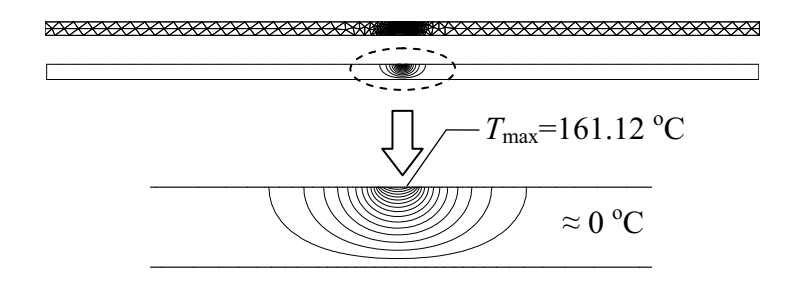


Fig. 34. Adaptive mesh and the temperature response at the heat source location.

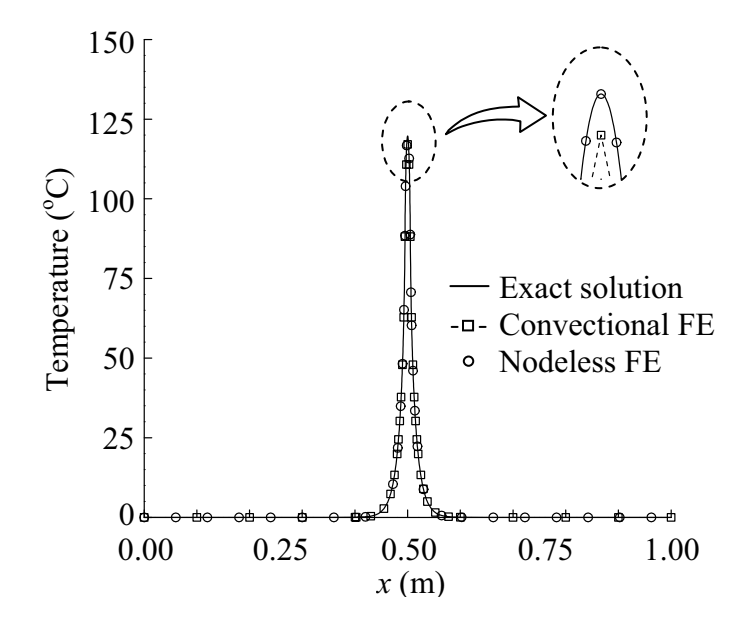


Fig. 35. Comparison of the exact temperature solution and the predicted temperature obtained from the combined adaptive meshing technique and the nodeless finite element method.

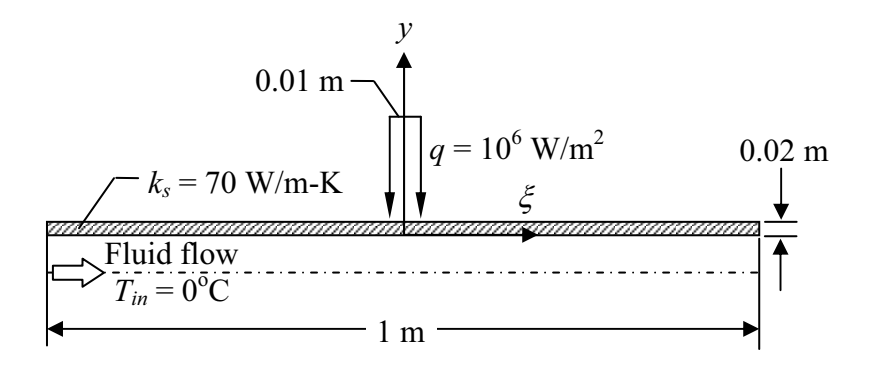


Fig. 36. Problem statement of a plate subjected intense heating with fluid flow beneath the plate.

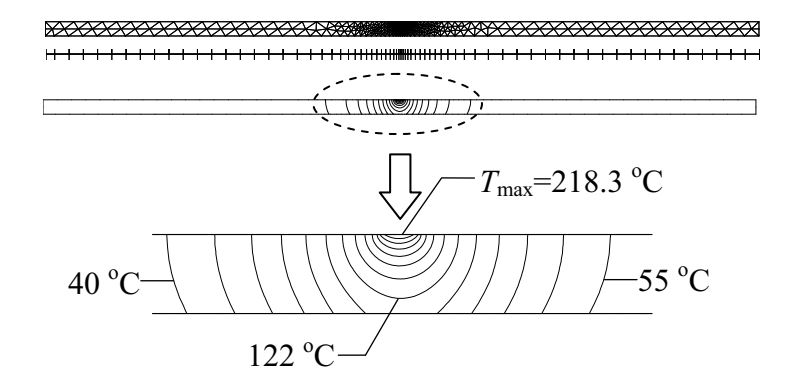


Fig. 37. Adaptive mesh and the temperature response at the heat source location.

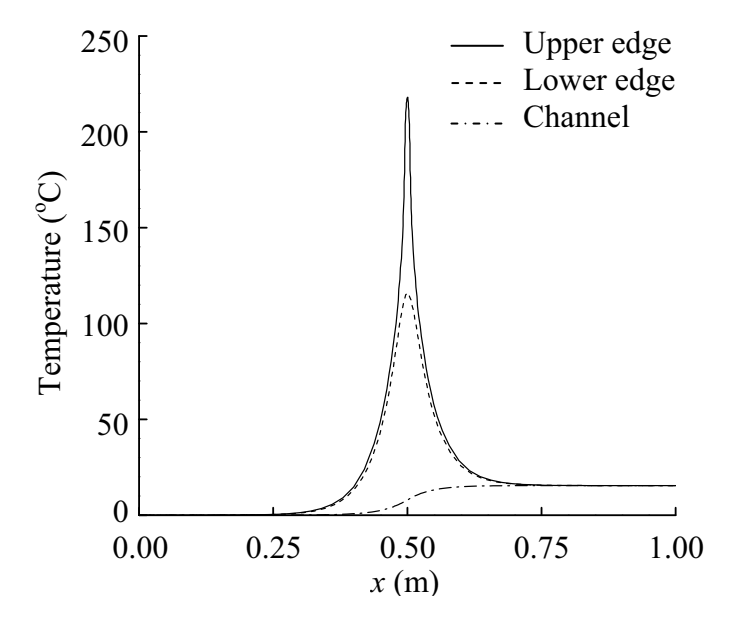


Fig. 38. Predicted temperature from the combined adaptive meshing technique and the nodeless finite element method.

Table 1. Comparison of the predicted peak temperatures obtained from the conventional and the nodeless variable finite element methods on both the uniform and adaptive meshes.

Mesh	Temperature (%Error)	
	Convectional	Nodeless
	FE	FE
Structured	117.094	119.773
	(2.169)	(0.070)
Adaptive	119.061	119.688
	(0.526)	(0.002)

Structural Analysis

The finite element equations for solid mechanic problems can be derived by applying the method of weighted residuals to the governing differential equations of interest. As an example, the governing differential equations that represent the equilibrium conditions of a plate in two dimensions are,

$$\frac{\partial \{E_S\}}{\partial x} + \frac{\partial \{F_S\}}{\partial y} = 0 \tag{103}$$

where the flux vector components $\{E_S\}$ and $\{F_S\}$ contain the stress components given by,

$${E_S} = \begin{cases} \sigma_{xx} \\ \sigma_{xy} \end{cases}$$
 and ${F_S} = \begin{cases} \sigma_{xy} \\ \sigma_{yy} \end{cases}$ (104)

The stress components σ_{xx} , σ_{yy} and σ_{xy} are related to strain components by the Hooke's law,

$$\{\sigma\} = [C]\{\varepsilon\} \tag{105}$$

where $\{\sigma\}$ is the vector of the stress components, [C] is the matrix of the material elastic constants, and $\{\varepsilon\}$ is the vector of the strain components.

These equations are to be solved with the boundary conditions that may consist of: (a) the specified displacements, u and v, in the x- and y-directions, respectively,

$$u = u(x, y)$$
 ; $v = v(x, y)$ (106)

and (b) the specified boundary tractions, T_{Sx} and T_{Sy} , in the x- and y-directions, respectively,

where n_x and n_y are direction cosines of the unit vector normal to the boundary.

Nodeless Variable Flux-Based Finite Element Formulation

The flux-based formulation is implemented to derive the corresponding finite element equations for the nodeless variable structural finite element. For the triangular element shape, the distribution of displacements over the element in the *x*- and *y*-directions are assumed in the form,

$$u(x,y) = \sum_{i=1}^{6} N_i(x,y)u_i(t) = \lfloor N(x,y) \rfloor \{u\}$$
 (108)

$$v(x,y) = \sum_{i=1}^{6} N_i(x,y)v_i(t) = \lfloor N(x,y) \rfloor \{v\}$$
 (109)

where $\lfloor N(x,y) \rfloor$ consists of the element interpolation functions; $\{u\}$ and $\{v\}$ are the vectors of the unknown displacements and the nodeless variables. The nodeless variable interpolation functions implemented in this paper are,

$$N_4 = L_2 L_3$$
 ; $N_5 = L_1 L_3$; $N_6 = L_1 L_2$ (110)

Each nodeless variable interpolation function varies quadratically along one edge and vanishes along the other edges. To derive the finite element matrices using the flux-based formulation, the method of weighted residuals is first applied to Eq. (103),

$$\int_{\Omega} N_i \left(\frac{\partial \{E_S\}}{\partial x} + \frac{\partial \{F_S\}}{\partial y} \right) d\Omega = 0$$
 (111)

where Ω is the element domain. The Gauss's theorem is then applied to the flux derivative terms to yield,

$$\int_{\Omega} N_i \frac{\partial \{E_S\}}{\partial x} d\Omega = \int_{S} N_i \{E_S\} n_x d\Gamma - \int_{\Omega} \frac{\partial N_i}{\partial x} \{E_S\} d\Omega$$
 (112)

$$\int_{\Omega} N_i \frac{\partial \{F_S\}}{\partial y} d\Omega = \int_{S} N_i \{F_S\} n_y d\Gamma - \int_{\Omega} \frac{\partial N_i}{\partial y} \{F_S\} d\Omega$$
 (113)

where S is the element boundary. Substituting Eqs. (112)-(113) into Eq. (111) to yield,

$$\int_{\Omega} \frac{\partial N_i}{\partial x} \{E_S\} d\Omega + \int_{\Omega} \frac{\partial N_i}{\partial y} \{F_S\} d\Omega = \int_{S} N_i \{E_S\} n_x d\Gamma + \int_{S} N_i \{F_S\} n_y d\Gamma$$
 (114)

The compact form of Eq. (114) could be written as,

$$\int_{\Omega} [B_S]^T \{\sigma\} d\Omega = \int_{S} [N]^T \{T_S\} d\Gamma$$
(115)

where

$$[B_S] = \begin{bmatrix} \frac{\partial N_1}{\partial x} & 0 & \frac{\partial N_6}{\partial x} & 0\\ 0 & \frac{\partial N_1}{\partial y} & \cdots & 0 & \frac{\partial N_6}{\partial y} \\ \frac{\partial N_1}{\partial y} & \frac{\partial N_1}{\partial x} & \frac{\partial N_6}{\partial y} & \frac{\partial N_6}{\partial x} \end{bmatrix}^T$$
(116)

$$[N] = \begin{bmatrix} N_1 & 0 & \dots & N_6 & 0 \\ 0 & N_1 & 0 & N_6 \end{bmatrix}$$
 (117)

$$\{\sigma\} = \begin{bmatrix} \sigma_{xx} & \sigma_{yy} & \sigma_{xy} \end{bmatrix}^T \tag{118}$$

$$\{T_S\} = \left| T_x \quad T_y \right|^T \tag{119}$$

In the flux-based formulation, the element flux distributions are computed from the nodal fluxes as,

$$\{\sigma\} = \left[\overline{N}\right]\!\left\{\overline{\sigma}\right\} \tag{120}$$

where

$$\left[\overline{N}\right] = \begin{bmatrix} \left\{\overline{N}\right\}^T & \left\{\overline{0}\right\}^T & \left\{\overline{0}\right\}^T \\ \left\{\overline{0}\right\}^T & \left\{\overline{N}\right\}^T & \left\{\overline{0}\right\}^T \\ \left\{\overline{0}\right\}^T & \left\{\overline{0}\right\}^T & \left\{\overline{N}\right\}^T \end{bmatrix}$$
(121)

$$\{\overline{\sigma}\} = \begin{cases} \{\sigma_{xx}\}_{1,2,3} \\ \{\sigma_{yy}\}_{1,2,3} \\ \{\sigma_{xy}\}_{1,2,3} \end{cases}$$

$$(122)$$

and the vectors $\{\overline{N}\}^T$ and $\{\overline{0}\}^T$ are

$$\left\{ \overline{N} \right\}^T = \left\lfloor N_1 \quad N_3 \quad N_3 \right\rfloor \tag{123}$$

$$\left\{\overline{0}\right\}^T = \left|\begin{array}{ccc} 0 & 0 & 0 \end{array}\right| \tag{124}$$

By following the same idea, the boundary tractions $\{T_S\}$ could be written as,

$$\{T_{\rm s}\} = \left[\overline{N}\right]\!\left\{\overline{T}_{\rm s}\right\} \tag{125}$$

where $[\overline{N}]$ and $\{\overline{T}_S\}$ are interpolation matrix and boundary tractions vector defined at the element boundary, respectively. The interpolation functions in Eq. (125) needed for integration along the element side S are,

$$N_1 = 1 - \frac{x}{L}$$
 ; $N_2 = \frac{x}{L}$; $N_3 = \frac{x}{L} \left(1 - \frac{x}{L} \right)$ (126)

where L is the length of element edge and x is the local coordinate along the edge. Substituting Eqs. (120) and (125) into Eq. (115), the finite element equations for the element are,

$$\int_{\Omega} [B_S]^T [\overline{N}] d\Omega \{\overline{\sigma}\} = \int_{S} [N]^T [\overline{N}] d\Gamma \{\overline{T}_S\}$$
(127)

Appropriate boundary conditions of the given problem are then applied. Finally, the system equations are iteratively solved for the nodal displacements and the nodeless variables using the preconditioned conjugate gradients method with an element-by-element approximation. The method is used to analyze the deformed shape and the stress distribution in an L-shape plate under uniform loading along the left edge as shown in Fig. 39. Figure 40 shows both the structured and unstructured meshes used in the analysis. The lower-right insert of Fig. 40 also shows an adaptive mesh that has small clustered elements near the plate corner to provide stress solution accuracy for this problem.

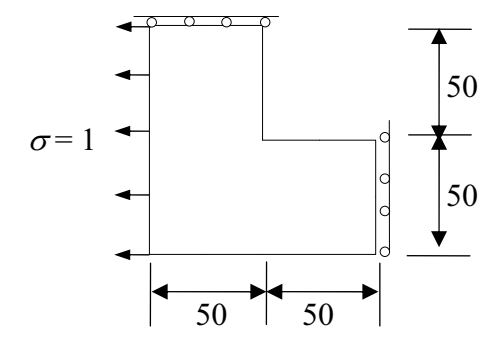


Fig. 39. Problem statement of L-shape domain.

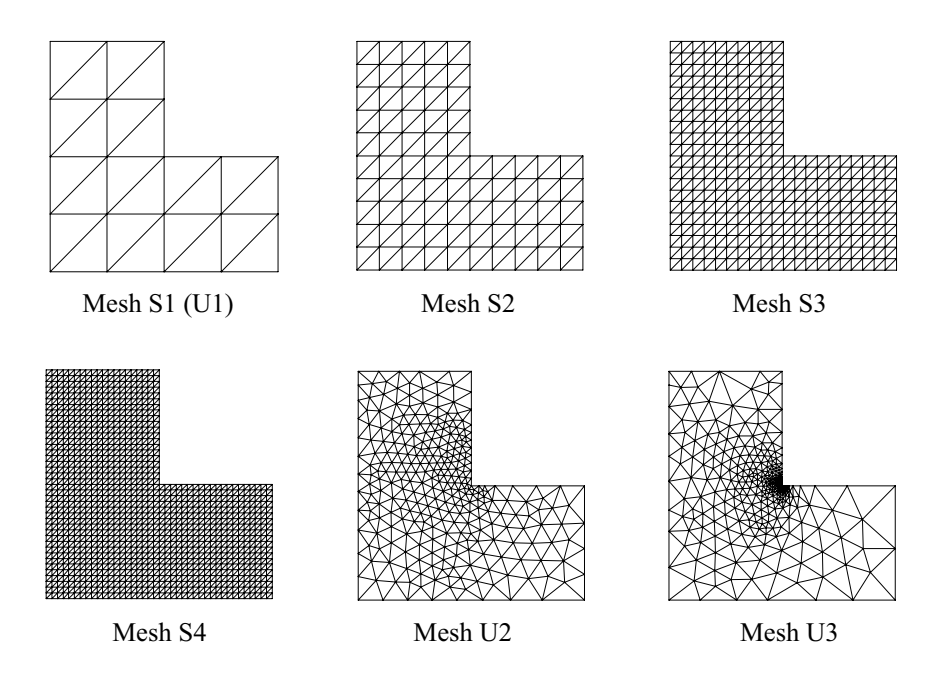


Fig. 40. Uniformly refined meshes and adaptive meshes used in the analysis of L-shape plate under uniform loading along the left edge.

The J and Domain Integral Technique for Crack Problems

Under the quasi-static analysis with crack lying on the x_1 axis, the two dimensional J-integral is defined by,

$$J = \lim_{\Gamma \to 0} \int_{\Gamma} (W \delta_{1i} - \sigma_{ij} u_{j,1}) n_i dC$$
 (128)

where Γ is a limiting contour starting from the bottom crack face and ending at the top surface, W is the strain energy density, σ_{ij} are the stress tensors, u_i are the displacement vectors, δ_{ij} is the Kronecker's delta, and n_i is the outward normal vector to the vanishing contour Γ . In the absence of crack face tractions, Eq. (128) for the closed curve $C = C_1 - \Gamma + C^+ + C^-$ can be written in the form,

$$J = \int_{C} (\sigma_{ij} u_{j,1} - W \delta_{1i}) m_i q_1 dC$$
 (129)

where q_1 is any sufficiently smooth function in the region enclosed by C provided that it is unity on Γ and zero on C_1 , and m_i is the outward normal vector to the domain surrounded by C. With the presence of thermal strain, the total strain tensor ε_{ij} could be presented as the sum of the mechanical and the thermal strains, $\varepsilon_{ij} = \varepsilon_{ij}^m + \beta T \, \delta_{ij}$, where ε_{ij}^m represents the mechanical strain, β is the coefficient of thermal expansion and T is the temperature relative to the reference state. Under the assumptions of the equilibrium conditions without the body forces and the strain energy density being only function of the mechanical strains, the divergence theorem is applied to Eq. (129) to yield the domain integral form,

$$J = \int_{A} \left[\left(\sigma_{ij} u_{j,1} - W \delta_{1i} \right) q_{1,i} + \beta t r(\sigma) T_{,1} q_{1} \right] dA$$
 (130)

where A is the area enclosed by C including the crack tip region as $\Gamma \to 0$, and $tr(\sigma)$ denotes the trace of σ_{ii} .

Typical solutions are illustrated by the problem of the compact tension specimen under loading in Figs. 41-43. The problem statement of the compact tension specimen is given in Fig. 41, while an adaptive finite element mesh is shown in Fig. 42. Figure 43 shows a good agreement of the computed *J*-integrals obtained from the adaptive finite element method and an estimation method.

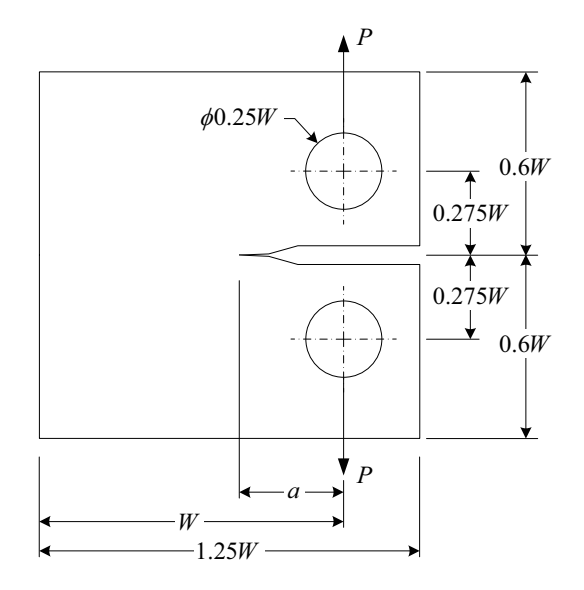


Fig. 41. The compact tension specimen.

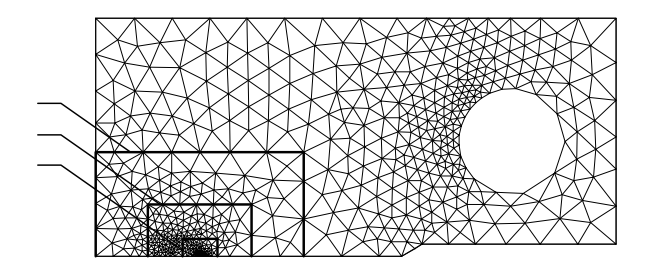


Fig. 42. The final adaptive mesh of the compact tension specimen with three integration domains.

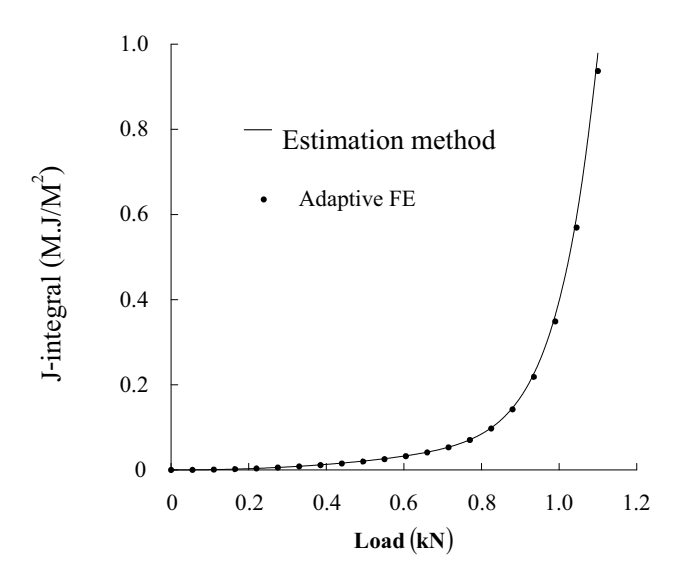


Fig. 43. Comparison of J-integrals from adaptive finite element and estimation methods for the compact tension specimen.

Application of the adaptive meshing technique has been extended to the analysis of built-up structures. The method is combined with the Discrete Kirchhoff Triangle (DKT) elements to analyze the bending behavior of the plates normally found in the built-up structure. The governing differential equations for in-plane deformation and bending behavior of the plate are given as follows.

The equations for the in-plane deformation are governed by the twodimensional equilibrium equations after neglecting the in-plane body forces as,

$$\frac{\partial \sigma_x}{\partial x} + \frac{\partial \tau_{xy}}{\partial y} = 0 \tag{131}$$

$$\frac{\partial \tau_{xy}}{\partial x} + \frac{\partial \sigma_{y}}{\partial y} = 0 \tag{132}$$

For the plane stress case, the stress components σ_x , σ_y and τ_{xy} are related to the strain components by Hooke's law as,

$$\{\sigma\} = [C]\{\varepsilon - \varepsilon_0\} \tag{133}$$

where $\{\sigma\}$, $\{\varepsilon\}$ and the thermal strain $\{\varepsilon_0\}$ vectors are defined by,

$$\left\{\sigma\right\}^{T} = \left|\begin{array}{ccc}\sigma_{x} & \sigma_{y} & \tau_{xy}\end{array}\right| \tag{134}$$

$$\left\{\varepsilon\right\}^{T} = \begin{vmatrix} \frac{\partial u}{\partial x} & \frac{\partial v}{\partial y} & \frac{\partial u}{\partial y} + \frac{\partial v}{\partial x} \end{vmatrix}$$
 (135)

$$\left\{\varepsilon_{0}\right\}^{T} = \left\{\alpha\right\}^{T} \left(T(x, y) - T_{0}\right) \tag{136}$$

The material stiffness matrix [C] is given by,

$$[C] = \frac{E}{1 - v^2} \begin{bmatrix} 1 & v & 0 \\ v & 1 & 0 \\ 0 & 0 & \frac{1 - v}{2} \end{bmatrix}$$
 (137)

and the vector for the coefficient of the thermal expansion $\{\alpha\}$ is defined by,

$$\left\{\alpha\right\}^{T} = \left|\begin{array}{ccc} \alpha & \alpha & 0 \end{array}\right| \tag{138}$$

The equation for the transverse deflection w in the z-direction normal to the x-y plane of a thin plate with the temperature T(z) through its thickness t is given by the equilibrium equation,

$$D\left(\frac{\partial^4 w}{\partial x^4} + \frac{2\partial^4 w}{\partial x^2 \partial y^2} + \frac{\partial^4 w}{\partial y^4}\right) = -\frac{1}{1 - \nu} \left(\frac{\partial^2 M_T}{\partial x^2} + \frac{\partial^2 M_T}{\partial y^2}\right) + p(x, y)$$
(139)

where p(x, y) is the applied lateral load normal to the plate, v is Poisson's ratio and D is the bending rigidity. The bending rigidity is defined by,

$$D = \frac{Et^3}{12(1 - v^2)} \tag{140}$$

where E is the modulus of elasticity, t is the thickness of the plate. The thermal moment M_T in Eq. (139) is defined,

$$M_T = E\alpha \int_{-t/2}^{t/2} (T(z) - T_0) z \, dz \tag{141}$$

The Constant Strain Triangle (CST) and the Discrete Kirchoff Triangle (DKT) finite elements are used for the in-plane deformation and the transverse deflection, respectively, as explained below.

The CST element assumes a linear distribution of the displacement components over the element. The finite element equations can be derived by applying the method of weighted residuals to the governing differential equations, Eqs. (131) and (132), which leads to the finite element equations in the form,

$$[K_m]\{\delta_m\} = \{F\} + \{F_m\}$$

$$(142)$$

where the vector $\{\delta_m\}$ contains the element nodal unknowns of the in-plane displacements in the element local x-y coordinates. The unknowns are the two in-plane displacements u and v for each node, thus, there are six unknowns per element. The element stiffness matrix $[K_m]$ appearing in Eq. (142) is defined by,

$$[K_m] = [B_m]^T [C_m][B_m] t A$$

$$(143)$$

where $[B_m]$ is the strain-displacement interpolation matrix. The vector $\{F\}$ on the right-hand-side of Eq. (142) contains the applied mechanical forces at element nodes. The vector $\{F_m\}$ consists of the equivalent nodal forces due to the thermal load defined by,

$$\{F_m\} = \left[B_m\right]^T \left[C_m\right] \{\alpha\} \left(T_{avg} - T_0\right) tA \tag{144}$$

The DKT element assumes a cubic distribution of the transverse deflection over the element. The finite element equations can be derived by applying the method of weighted residuals to the plate bending equation, Eq. (139), which leads to the finite element equations in the form,

$$[K_b]\{\delta_b\} = \{F_p\} + \{F_b\} \tag{145}$$

where the vector $\{\delta_b\}$ contains the element nodal unknowns of the transverse deflections and rotations. Each node has a transverse deflection in z-direction and two rotations about x- and y- directions. Thus there are nine degrees of freedom per element. The element stiffness matrix $[K_B]$ and the nodal force vector due to the applied loads $\{F_p\}$ are defined by,

$$[K_b] = \int_A [B_b]^T [D] [B_b] dA$$
 (146)

$$\left\{ F_{p}\right\} = \int_{A} \left[N_{p} \right]^{T} p dA \tag{147}$$

where the strain-displacement interpolation matrix $[B_b]$ is,

$$\begin{bmatrix} B_{b} \end{bmatrix} = \frac{1}{2A} \begin{bmatrix} y_{31} \left\lfloor \frac{\partial H_{x}}{\partial \xi} \right\rfloor + y_{12} \left\lfloor \frac{\partial H_{x}}{\partial \eta} \right\rfloor \\ -x_{31} \left\lfloor \frac{\partial H_{y}}{\partial \xi} \right\rfloor - x_{12} \left\lfloor \frac{\partial H_{y}}{\partial \eta} \right\rfloor \\ -x_{31} \left\lfloor \frac{\partial H_{x}}{\partial \xi} \right\rfloor - x_{12} \left\lfloor \frac{\partial H_{x}}{\partial \eta} \right\rfloor + y_{31} \left\lfloor \frac{\partial H_{y}}{\partial \xi} \right\rfloor + y_{12} \left\lfloor \frac{\partial H_{y}}{\partial \eta} \right\rfloor \end{bmatrix} \tag{148}$$

where $\left\{\frac{\partial H_x}{\partial \xi}\right\}, \left\{\frac{\partial H_y}{\partial \xi}\right\}, \left\{\frac{\partial H_x}{\partial \eta}\right\}$ and $\left\{\frac{\partial H_y}{\partial \eta}\right\}$ are given by,

$$\left\{ \frac{\partial H_x}{\partial \xi} \right\} =
\begin{cases}
P_6(1-2\xi) + \eta(P_5 - P_6) \\
q_6(1-2\xi) - \eta(q_5 + q_6) \\
-4 + 6(\xi + \eta) + r_6(1-2\xi) - \eta(r_5 + r_6) \\
-P_6(1-2\xi) + \eta(P_4 + P_6) \\
q_6(1-2\xi) + \eta(q_4 - q_6) \\
-2 + 6\xi + r_6(1-2\xi) + \eta(r_4 - r_6) \\
-\eta(P_4 + P_5) \\
\eta(q_4 - q_5) \\
\eta(r_4 - r_5)
\end{cases}$$
(149)

$$\left\{ \frac{\partial H_{y}}{\partial \xi} \right\} = \begin{cases}
t_{6}(1-2\xi) + \eta(t_{5}-t_{6}) \\
1 + r_{6}(1-2\xi) - \eta(r_{5}+r_{6}) \\
-q_{6}(1-2\xi) + \eta(q_{5}+q_{6}) \\
-t_{6}(1-2\xi) + \eta(t_{4}+t_{6}) \\
-1 + r_{6}(1-2\xi) + \eta(r_{4}-r_{6}) \\
-q_{6}(1-2\xi) - \eta(q_{4}-q_{6}) \\
-\eta(t_{4}+t_{5}) \\
\eta(r_{4}-r_{5}) \\
-\eta(q_{4}-q_{5})
\end{cases} (150)$$

$$\left\{ \frac{\partial H_{x}}{\partial \eta} \right\} = \left\{ \begin{array}{l}
-P_{5}(1-2\eta) + \xi(P_{5}-P_{6}) \\
q_{5}(1-2\eta) - \xi(q_{5}+q_{6}) \\
-4 + 6(\xi+\eta) + r_{5}(1-2\eta) - \xi(r_{5}+r_{6}) \\
\xi(P_{4}+P_{6}) \\
\xi(q_{4}-q_{6}) \\
\xi(r_{4}-r_{6}) \\
P_{5}(1-2\eta) - \xi(P_{4}+P_{5}) \\
q_{5}(1-2\eta) + \xi(q_{4}-q_{5}) \\
-2 + 6\eta + r_{5}(1-2\eta) + \xi(r_{4}-r_{5})
\end{array} \right\} \tag{151}$$

$$\left\{ \frac{\partial H_{y}}{\partial \eta} \right\} = \begin{cases}
-t_{5}(1-2\eta) + \xi(t_{5}-t_{6}) \\
1 + r_{5}(1-2\eta) - \xi(r_{5}+r_{6}) \\
-q_{5}(1-2\eta) + \xi(q_{5}+q_{6}) \\
\xi(t_{4}+t_{6}) \\
\xi(r_{4}-r_{6}) \\
-\xi(q_{4}-q_{6}) \\
t_{5}(1-2\eta) - \xi(t_{4}+t_{5}) \\
-1 + r_{5}(1-2\eta) - \xi(q_{4}-q_{5})
\end{cases}$$
(152)

The coefficients P_k , q_k , r_k and t_k ; k = 4, 5, 6 depend on the element shape and are given by,

$$P_{k} = \frac{-6x_{ij}}{\ell_{ii}^{2}}$$
 (153);
$$q_{k} = \frac{3x_{ij}y_{ij}}{\ell_{ii}^{2}}$$
 (154)

$$P_{k} = \frac{-6x_{ij}}{\ell_{ij}^{2}}$$

$$(153); q_{k} = \frac{3x_{ij}y_{ij}}{\ell_{ij}^{2}}$$

$$(154)$$

$$r_{k} = \frac{3y_{ij}^{2}}{\ell_{ij}^{2}}$$

$$(155); t_{k} = \frac{-6y_{ij}}{\ell_{ij}^{2}}$$

$$(156)$$

where

$$\ell_{ii} = \sqrt{x_{ii}^2 + y_{ii}^2} \tag{157}$$

The coefficients x_{ij} and y_{ij} , i, j = 1, 2, 3 are defined in terms of the element nodal coordinates,

$$x_{ij} = x_i - x_j$$
 (158); $y_{ij} = y_i - y_j$ (159)

and the plate material stiffness matrix [D] in Eq. (146) is defined by,

$$[D] = \frac{Et^3}{12(1-\nu^2)} \begin{bmatrix} 1 & \nu & 0 \\ \nu & 1 & 0 \\ 0 & 0 & \frac{1-\nu}{2} \end{bmatrix}$$
 (160)

The above finite element matrices are in closed-form so that they can be implemented in the computer program directly.

The vector of the equivalent nodal forces due to the temperature change $\{F_b\}$ in Eq. (145) is defined by,

$$\left\{ F_{b}\right\} = \int_{A} \left[B_{b}\right]^{T} \left\{M\right\} dA \tag{161}$$

where the vector $\{M\}$ is given by,

$$\{M\} = | M_T \quad M_T \quad 0 | \tag{142}$$

The vector of the equivalent nodal forces due to the thermal load $\{F_b\}$ can be derived in closed-form as,

$$\left\{ F_{b} \right\} = M_{T} \left[G \right]^{T} \begin{Bmatrix} 1 \\ 1 \\ 0 \end{Bmatrix} \tag{163}$$

where the matrix [G] is,

$$[G] = \frac{1}{6} \begin{bmatrix} y_{31} \lfloor G_{11} \rfloor + y_{12} \lfloor G_{12} \rfloor \\ -x_{31} \lfloor G_{21} \rfloor - x_{12} \lfloor G_{22} \rfloor \\ -x_{31} \lfloor G_{11} \rfloor - x_{12} \lfloor G_{12} \rfloor + y_{31} \lfloor G_{21} \rfloor + y_{12} \lfloor G_{22} \rfloor \end{bmatrix}$$

$$(164)$$

The coefficients x_{ij} and y_{ij} , i, j = 1, 2, 3 are given in Eqs. (158) - (159). The row matrices $[G_{ij}]$; i, j = 1, 2, in Eq. (164) are given by,

$$\begin{bmatrix} G_{11} \end{bmatrix} = \begin{bmatrix} p_5 & -q_5 & -r_5 & p_4 & q_4 & r_4 & (-p_4 - p_5) \\ (q_4 - q_5) & (r_4 - r_5) \end{bmatrix}$$
(165)

$$\begin{bmatrix} G_{12} \end{bmatrix} = \begin{bmatrix} -p_6 & -q_6 & -r_6 & (p_4 + p_6) & (q_4 - q_6) \\ (r_4 - r_6) & -p_4 & q_4 & r_4 \end{bmatrix}$$
(166)

$$\begin{bmatrix} G_{21} \end{bmatrix} = \begin{bmatrix} t_5 & (3 - r_5) & q_5 & t_4 & (-3 + r_4) & -q_4 \\ (-t_4 - t_5) & (r_4 - r_5) & (-q_4 + q_5) \end{bmatrix}$$
(167)

where the coefficients P_k , q_k , r_k and t_k ; k = 4, 5, 6 are given in Eqs. (153)-(157).

To demonstrate the capability of the adaptive meshing technique for thermal stress analysis of a complex plate structure, the three-dimensional built-up structure with intersection panels is considered. The localized heating results in high temperature gradients and attendant thermal stresses in the structure. Both structure temperature and boundary conditions are prescribed as shown in Fig. 44. The peak temperature of 390 K is assumed in the two hot spot regions with the temperature distributions. Away from these hot spot regions, the structure temperature is closed to the surrounding medium temperature of 55 K.

A fine finite element model is first constructed as shown in Fig. 45(a). The model consists of 3,168 nodes and 6,114 triangular elements. The predicted stress distribution in the Y-direction superimposed on the deformed geometry is shown in Fig. 45(b). The high compressive stress with a magnitude of 172 MPa is at the two hot spot regions. However, a quite higher tensile stress with a magnitude of 372 MPa occurs between these two hot spot regions. This fine finite element model requires a large computational time as well as the computer memory. These difficulties can be alleviated and the analysis computational time can be reduced by the use of the adaptive meshing technique.

Application of the adaptive meshing technique starts from constructing a fairly uniform mesh as shown in Fig. 46(a). The initial mesh consists of 547 nodes and 994 triangular elements. With this mesh, the predicted thermal stress distribution on the deformed geometry is shown in Fig 47(a). The peak compressive stress at the two hot spots is 138 MPa while the peak tensile stress between both hot spots is 228 MPa. The temperature and the stress distributions (in the form of Von Mises stress) obtained from the initial mesh are used as the meshing parameters to construct a new adaptive mesh, shown in Fig. 46(b), with 528 nodes and 989 elements. The finer elements are concentrated in the high stress regions on the panels to provide accurate solution. Coarser elements are generated in other regions to reduce the problem size and computational time. The predicted thermal stress distribution in the Y-direction superimposed on the deformed geometry is shown in Fig. 47(b). The figure

shows that the adaptive mesh model can provide the same stress solution accuracy as those obtained from the fine mesh model.

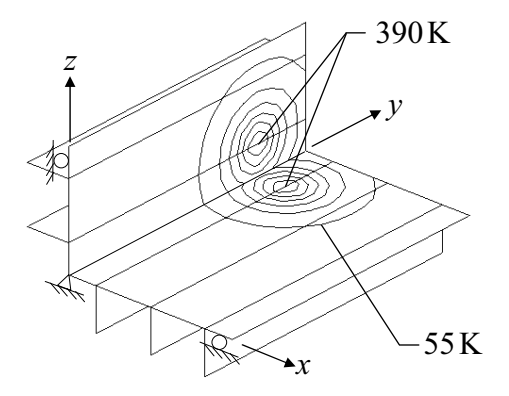


Fig. 44. Boundary conditions and temperature distributions for the intersection panels

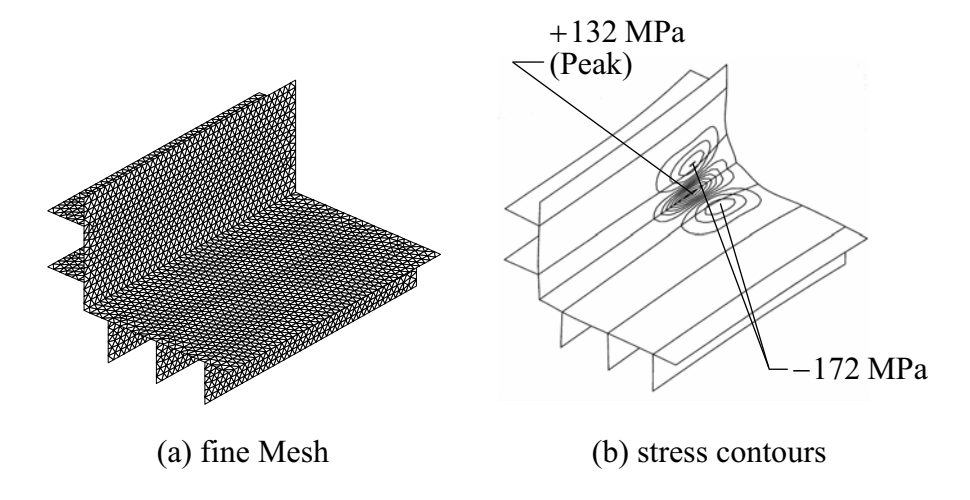


Fig. 45. Fine finite element mesh and predicted axial stress contours on deformed configuration.

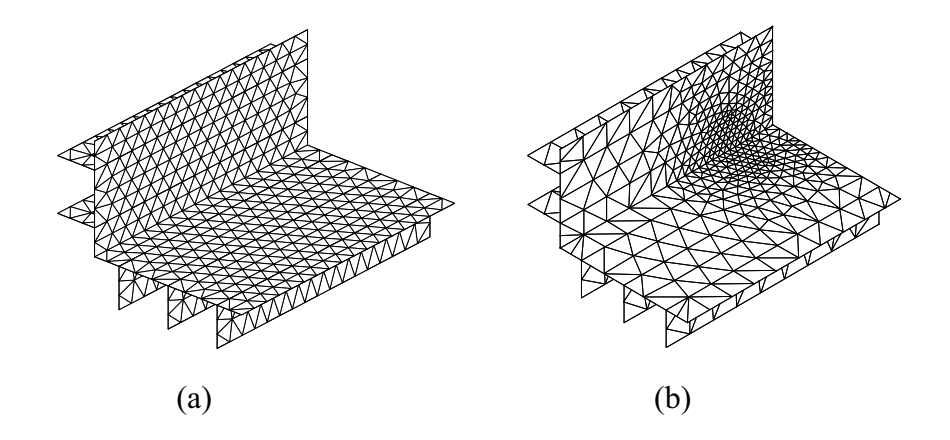


Fig. 46. Finite element meshes for intersection panel: (a) initial mesh and (b) adaptive mesh.

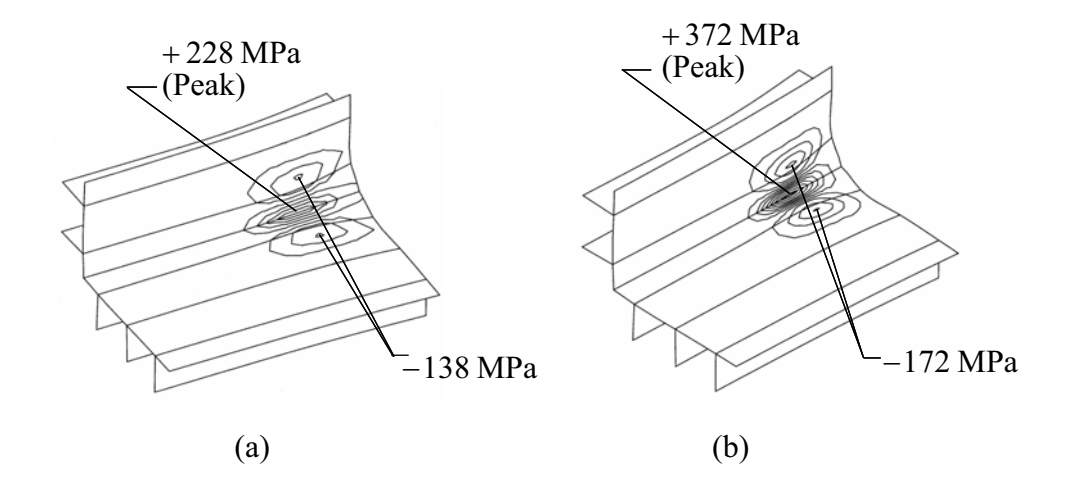


Fig. 47. Predicted axial stress contours from: (a) initial mesh and (b) adaptive mesh.

Fluid-Thermal-Structural Interaction

The governing equations for conjugate heat transfer between the solid and fluid flow consist of the conservation of mass which is called the continuity equation, the conservation of momentum in x- and y- directions, and the conservation of energy, as follows,

Continuity equation,

$$\frac{\partial u}{\partial x} + \frac{\partial v}{\partial y} = 0 \tag{169a}$$

Momentum equations,

$$\rho \left[u \frac{\partial u}{\partial x} + v \frac{\partial u}{\partial y} \right] = -\frac{\partial p}{\partial x} + \mu \left[\frac{\partial^2 u}{\partial x^2} + \frac{\partial^2 u}{\partial y^2} \right]$$
 (169b)

$$\rho \left[u \frac{\partial v}{\partial x} + v \frac{\partial v}{\partial y} \right] = -\frac{\partial p}{\partial y} + \mu \left[\frac{\partial^2 v}{\partial x^2} + \frac{\partial^2 v}{\partial y^2} \right] - pg \left(1 - \beta (T - T_0) \right)$$
 (169c)

Energy equation,

$$\rho c \left[u \frac{\partial T}{\partial x} + v \frac{\partial T}{\partial y} \right] = k \left[\frac{\partial^2 T}{\partial x^2} + \frac{\partial^2 T}{\partial y^2} \right] + \rho Q$$
 (169d)

where u and v are the velocity components in the x- and y- direction, respectively, ρ is the density, p is the pressure, μ is the viscosity, g is the gravitational acceleration constant, β is the volumetric coefficient of thermal expansion, T is the temperature, T_0 is the reference temperature for which buoyant force in the y-direction vanishes, c is the specific heat, k is the coefficient of thermal conductivity and Q is the internal heat generation rate per unit volume. Equation (169d) can be used for solving conduction heat transfer in solid by setting both the velocity components, u and v, as zero.

Finite Element Formulation

The three-node triangular element is used in this study. The element assumes linear interpolation functions for the velocity components, the pressure, and the temperature as,

$$u(x,y) = \sum N_i(x,y)u_i = \lfloor N \rfloor \{u\}$$
 (170a)

$$v(x,y) = \sum N_i(x,y)v_i = \lfloor N \rfloor \{v\}$$
 (170b)

$$p(x,y) = \sum N_i(x,y)p_i = \lfloor N \rfloor \{p\}$$
 (170c)

$$T(x,y) = \sum N_i(x,y)T_i = \lfloor N \rfloor \{T\}$$
 (170d)

where i = 1, 2, 3; and N_i is the element interpolation functions.

The basic idea of the solution algorithm presented herein is to use the two momentum equations for solving both of the velocity components, use the continuity equation for solving the pressure, and use the energy equation for solving the temperature in solid and fluid regions.

Streamline Upwind Petrov-Galerkin Method

The basic idea of the streamline upwind method is to include diffusion only in the flow direction. Extended to a Petrov-Galerkin formulation, the standard Galerkin weighting functions are modified by adding a streamline upwind perturbation, p, for suppressing the non-physical spatial oscillation in the numerical solution, which again acts only in the flow direction. Herein, the modified weighting function, W_i , can be expressed as,

$$W_{i} = N_{i} + p = N_{i} + \frac{\alpha h}{2|U|} \left[u \frac{\partial N_{i}}{\partial x} + v \frac{\partial N_{i}}{\partial y} \right]$$
 (171)

where α is calculated for each element from,

$$\alpha = \alpha_{opt} = \coth Pe - \frac{1}{Pe}$$
 (172a)

with Pe =
$$\frac{|U|h}{2\tilde{k}}$$
 and $|U| = \sqrt{u^2 + v^2}$ (172b)

where Pe is the Peclet numbers, $\left|U\right|$ is mean resultant velocity and h is element size.

A typical solution of a coupled fluid-structure heat transfer is shown by the problem in Figs. 48-49. Figure 48 describes the problem statement of a fluid circulation in a cavity with hot tube at the center and cold walls on both sides. The bottom edge of the cavity is insulated, while there is heat transfer to the solid along the top edge. Figure 49 shows the predicted temperature contours of the fluid and solid when the solid has different values of the thermal conductivity coefficient.

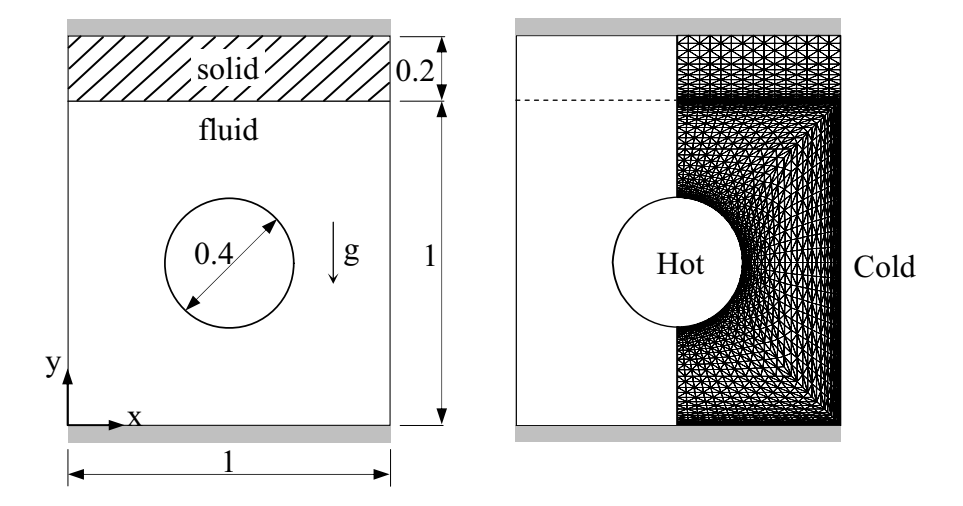


Fig. 48. Coupled fluid flow and heat transfer in solid.

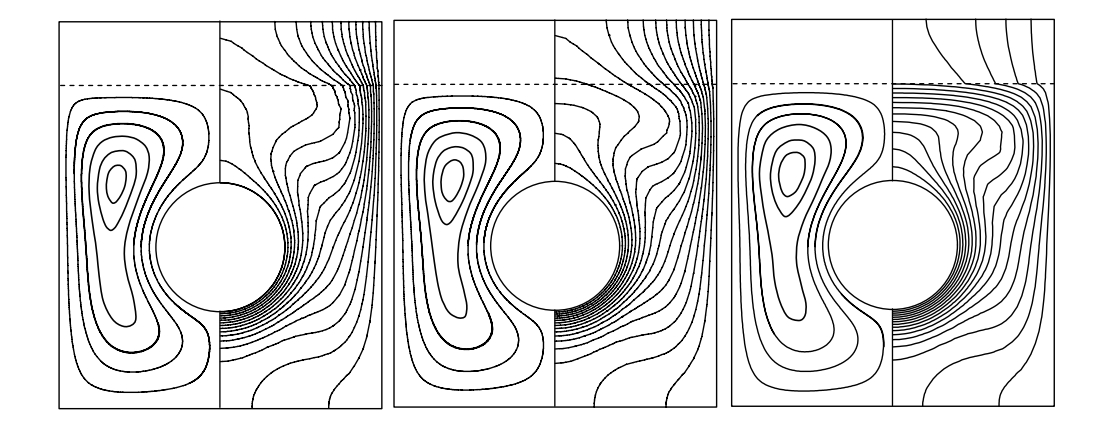


Fig. 49. Temperature contours at different solid thermal conductivities.

Figure 50 shows the problem statement of a free convection flow in an enclosure with fins. Along the lower and upper edges of the model, the temperatures are specified as 1 and 0, respectively, while both sides of the model are insulated. The objective is to investigate the flow behaviors of the fluids in both the lower and upper enclosures. The finite element model for the two fluid regions and the three fins is shown in Fig. 51. Figure 52 shows the predicted temperature distributions in both the fluid regions and the three fins. The predicted Von Mises stress distribution on the deformed shape of the fins is shown in Fig. 53.

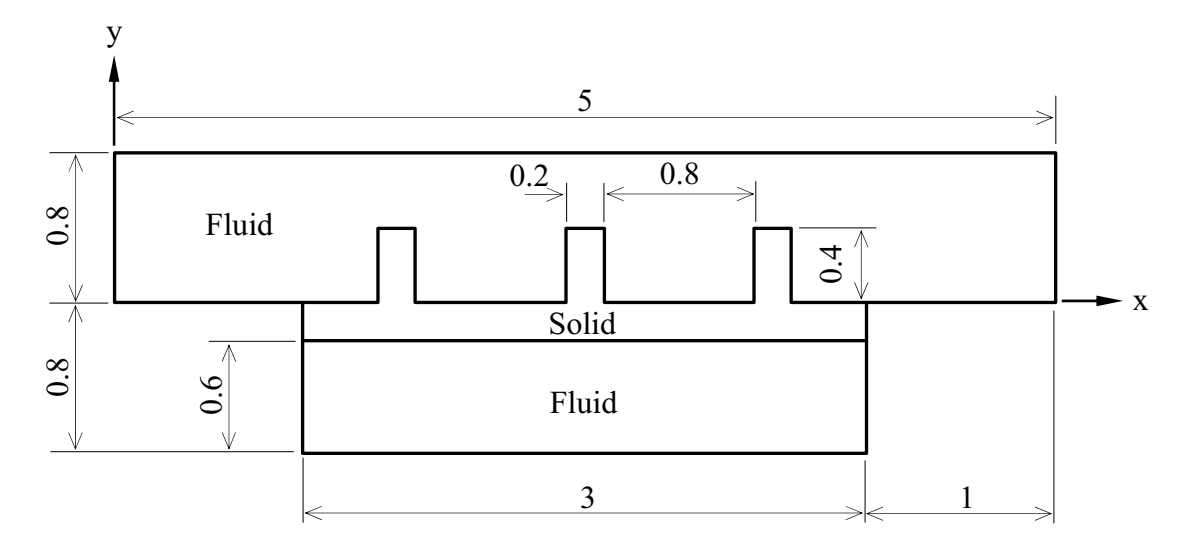


Fig. 50. Problem statement of free convection flow in enclosures with fins.

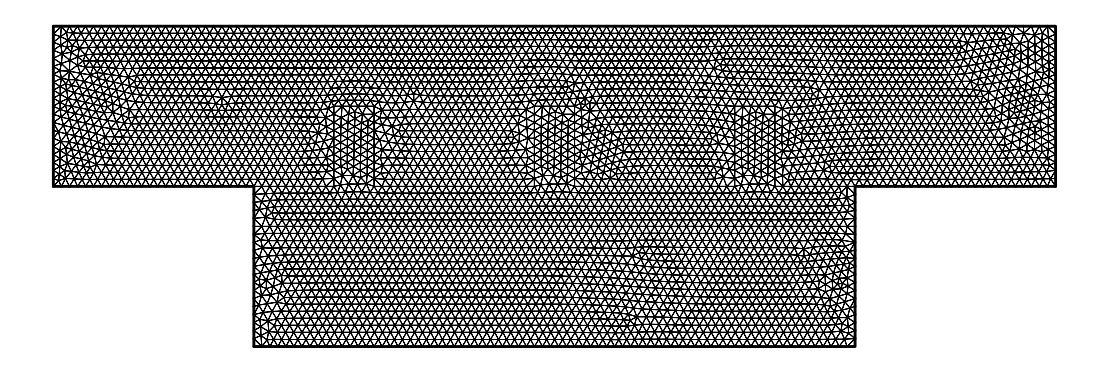


Fig. 51. Finite element model for fluid and structure of free convection flow in enclosures with fins.

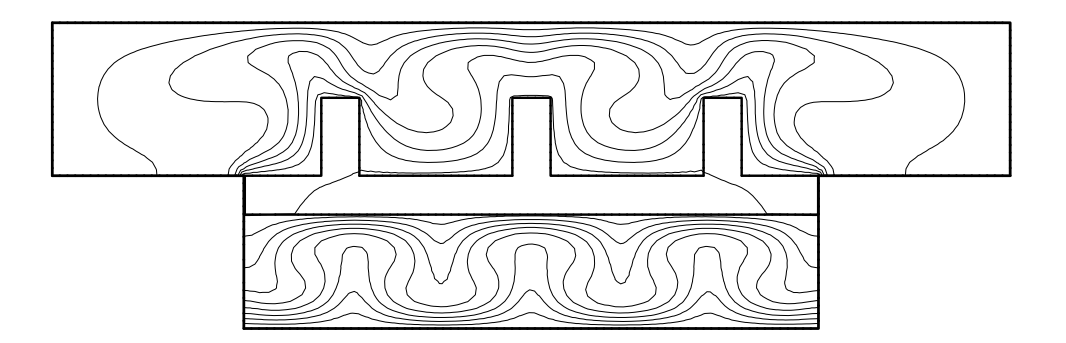


Fig. 52. Computed temperature distributions for the fluid and structure of free convection flow in enclosures with fins.

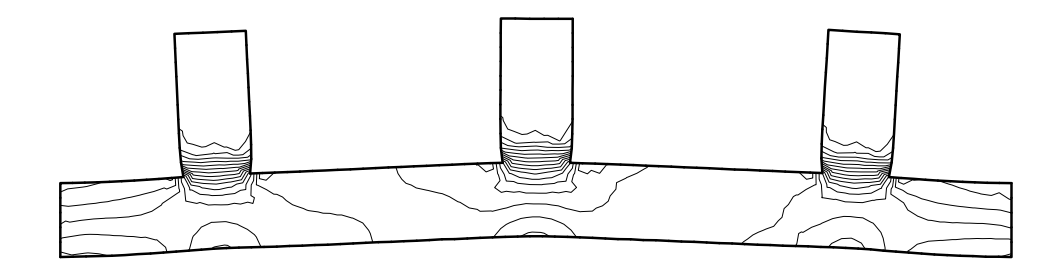


Fig. 53. Predicted Von Mises stress distribution on deformed fin shape for the problem of free convection flows in enclosures.

The high-speed compressible flow formulation is combined with the heat transfer and the structural analyses of the structure to demonstrate the fluid-thermal-structural interaction phenomena. Figure 54 shows the problem statement of a Mach 4 flow over a wedge in a channel. The flow creates a shock wave that impinges on a panel embedded in the upper wall of the channel. Figures 55(a) and (b) show an adaptive finite element mesh and the predicted density contours, respectively. The upper figure shows small clustered elements generated along the shock wave and in the boundary layers along both the wedge and the upper wall surfaces. The impingement of the shock on the panel causes the panel temperature to rise. The panel then bows into the free stream and alters the flow field. Figures 56(a) and (b) show the adaptive finite element mesh and the corresponding density contours after the panel has bowed and altered the flow field. This example clearly demonstrates the advantage of the adaptive finite element method for predicting the fluid, thermal and structural interaction phenomena.

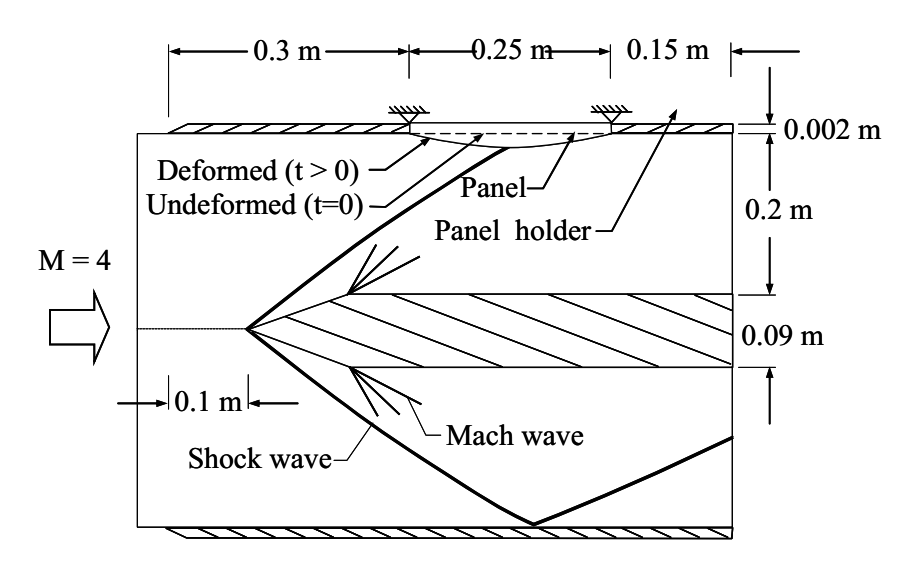


Fig. 54. A Mach 4 flow in a channel.

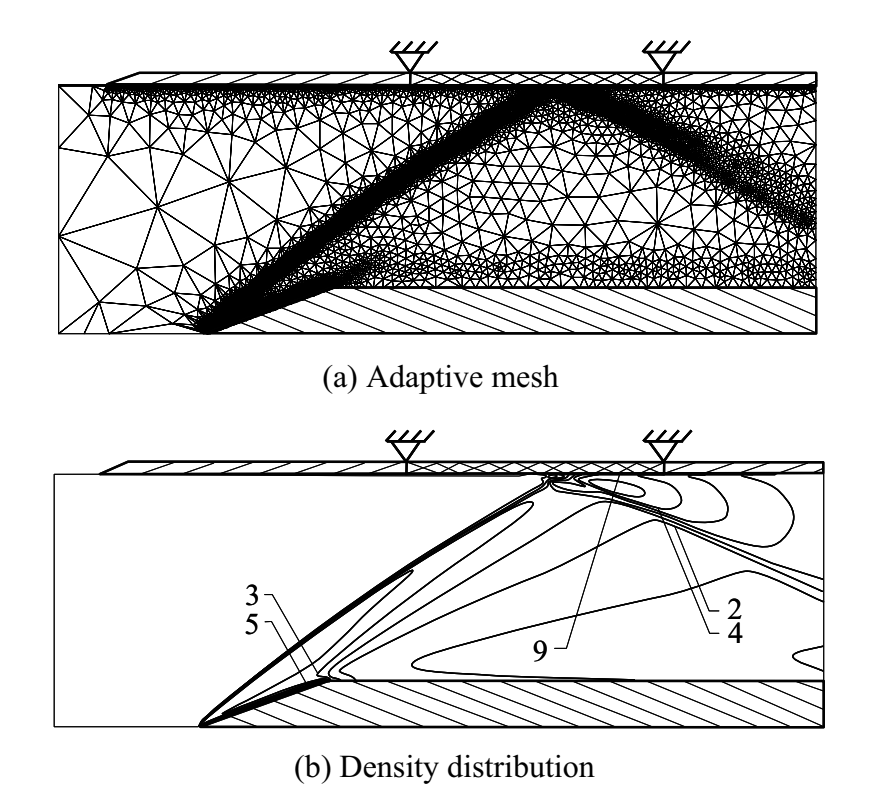


Fig. 55. Adaptive mesh and corresponding density contours (kg/m³) for a Mach 4 flow in a channel at initial time.

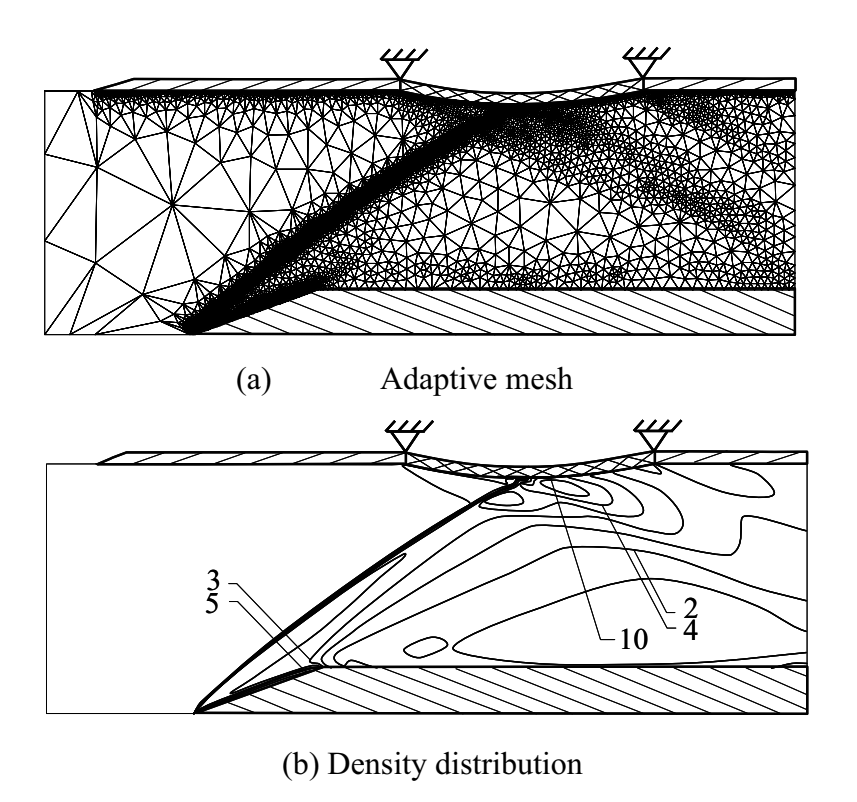


Fig. 56. Adaptive mesh and corresponding density contours for a Mach 4 flow in a channel with convex deformation at 60 seconds.

Output ที่ได้จากโครงการ

ผลลัพธ์ที่เกิดขึ้นจากโครงการ ประกอบด้วยผลงานที่ได้รับการตีพิมพ์ลงในวารสาร ระดับนานาชาติ ตำรา สิทธิบัตรที่ได้ยื่นจด รายชื่อนิสิตและนักศึกษาผู้สำเร็จการศึกษา รายชื่อ อาจารย์นักวิจัยใหม่ผู้ได้เลื่อนสถานะภาพทางวิชาการ ดังมีรายละเอียดต่อไปนี้

<u>ผลงานตีพิมพ์ในวารสารวิชาการนานาชาติ</u>

- 1. **Phongthanapanich, S.** and **Dechaumphai, P.**, "Adaptive Nodeless Variable Finite Elements with Flux-Based Formulation for Thermal-Structural Analysis", <u>Acta Mechanica Sinica Journal</u>, Vol. 24, No. 2, 2008, pp. 181-188. (impact factor = 0.865)
- Potjananapasiri, K, Phongthanapanich, S. and Dechaumphai, P., "J-Integral Calculation by Domain Integral Technique Using Adaptive Finite Element Method", <u>Structural Engineering & Mechanics</u>, <u>An International Journal</u>, Vol. 28, No. 4, 2008, pp. 461-477. (impact factor = 0.438)
- 3. **Phongthanapanich, S.** and **Dechaumphai, P.**, "Healing of Shock Instability for Roe's Flux-Difference Splitting Scheme on Triangular Meshes", <u>International Journal for Numerical Methods in Fluids</u>, Vol. 59, 2008, pp. 559-575. (*impact factor* = 0.936)
- 4. **Phongthanapanich, S.** and **Dechaumphai, P.**, "Nodeless Variable Finite Element Method for Stress Analysis Using Flux-Based Formulation", <u>Journal of Mechanical Science and Technology</u>, Vol. 22, No. 4, 2008, pp. 639-646. (*impact factor* = 0.374)
- 5. Trivivatana, S., **Phongthanapanich, S.** and **Dechaumphai, P.**, "Improved Numerical Solution Accuracy of Poisson's Equation by Adaptive Nodeless Variable Finite Elements with Flux-Based Formulation", <u>Transactions of the Canadian Society for Mechanical Engineering</u>, Vol. 32, No. 1, 2008, pp. 23-42. (impact factor = 0.195)

- 6. **Wansophark, W.** and **Dechaumphai, P.**, "Streamline Upwind Finite Element Method Using 6-Node Triangular Element with Adaptive Remeshing Technique for Convective-Diffusion Problems", <u>Applied Mathematics and Mechanics</u>, Vol. 29, No. 11, 2008, pp. 1-12. (*impact factor* = 0.393)
- 7. Suluksna, K. and **Juntasaro**, **E.**, "Assessment of Intermittency Transport Equations for Modeling Transition in Boundary Layers Subjected to Freestream Turbulence", <u>International Journal of Heat and Fluid Flow</u>, Vol. 29, 2008, pp. 48-61. (*impact factor* = 1.498)
- 8. **Phongthanapanich, S.** and **Dechaumphai, P.**, "A Characteristic-Based Finite Volume Method for Convection-Diffusion-Reaction Equation", <u>Transactions of the Canadian Society for Mechanical Engineering</u>, Vol. 32, No. 3-4, 2008, pp. 549-, 559. (impact factor = 0.195)
- 9. **Phongthanapanich, S.** and **Dechaumphai, P.**, "Finite Volume Method for Convection-Diffusion-Reaction Equation on Triangular Meshes", <u>International Journal for Numerical Methods in Biomedical Engineering</u>, (formerly: Communications in Numerical Methods in Engineering), Vol. 26, No. 6, 2008, pp. 716-727. (impact factor = 0.595)
- 10. Suluksna, K., **Dechaumphai, P.** and **Juntasaro, E.**, "Correlations for Modeling Transitional Boundary Layers under Influences of Freestream Turbulence and Pressure Gradient", <u>International Journal of Heat and Fluid Flow</u>, Vol. 30, 2009, pp. 66-75. (*impact factor* = 1.498)
- 11. **Phongthanapanich**, **S.** and **Dechaumphai**, **P.**, "Combined Finite Volume Element Method for Singularly Perturbed Reaction-Diffusion Problems", <u>Journal of Applied Mathematics and Computation</u>, Vol. 209, 2009, pp. 177-185. (impact factor = 0.684)
- 12. Sitprasert C., **Dechaumphai**, **P.** and **Juntasaro**, **V.**, "A Thermal Conductivity Model for Nanofluids Including Effect of the Temperature-Dependent Interfacial Layer", <u>Journal of Nanoparticle Research</u>, Vol. 11, 2009, pp. 1465-1476. (*impact factor* = 2.478)

- 13. **Phongthanapanich, S.** and **Dechaumphai, P.**, "Combined Finite Volume and Finite Element Method for Convection-Diffusion-Reaction Equation", <u>Journal of Mechanical Science and Technology</u>, Vol. 23, No. 3, 2009, pp. 790-801.
- 14. Tongkratoke, A., Chinnarasri, C., Pornprommin, A., **Dechaumphai, P.** and **Juntasaro, V.**, "Non-linear Turbulence Models for Multiphase Recirculating Free-Surface Flow Over Stepped Spillways", <u>International Journal of Computational Fluid Dynamics</u>, Vol. 23, No. 5, 2009, pp. 401-409. (*impact factor* = 0.571)
- 15. **Phongthanapanich, S.** and **Dechaumphai, P.**, "Finite Volume Element Method for Analysis of Unsteady Reaction-Diffusion Problems", <u>Acta Mechanica Sinica Journal</u>, Vol. 25, 2009, pp. 481-489. (impact factor = 0.865)
- 16. Reepolmaha, S., **Limtrakarn, W.**, Uthaisang-Tanechpongtamb, W. and **Dechaumphai, P.**, "Fluid Temperature at the Corneal Endothelium during Phacoemulsification: Comparison of an Ophthalmic Viscosurgical Device and Balanced Salt Solution using Finite Element Method", Ophthalmic Research, Vol. 43, No. 4, 2010, pp. 173-178. (impact factor = 1.288)
- 17. Malatip, A., **Wansophark, W.** and **Dechaumphai, P.**, "A Second-Order Time-Accurate Finite Element Method for Analysis of Conjugate Heat Transfer between Solid and Unsteady Viscous Flow", <u>Journal of Mechanical Science and Technology</u>, Vol. 23, No. 3, 2009, pp. 775-789. (*impact factor* = 0.374)
- 18. **Phongthanapanich, S.** and **Dechaumphai, P.**, "Explicit Characteristic Finite Volume Method for Convection-Diffusion Equation on Rectangular Grids", Accepted for publication in <u>Journal of Chinese Institute for Engineers</u>, 2010. (impact factor = 0.219)

- 19. **Limtrakarn, W.**, Yodsangkham, A., Namlaow A. and **Dechaumphai, P.**, "Determination of KI, KII and Trajectory of Initial Crack by Finite Element Method and Photoelastic Technique", <u>Experimental Techniques</u>, Wiley Interscience Online, doi: 10.1111/j.1747-1567, 2010, pp. 27-35. (impact factor = 0.500)
- 20. **Phongthanapanich, S.** and **Dechaumphai, P.**, "Explicit Characteristic Based Finite Volume Element Method for Level Set Equation", Accepted for publication in the <u>International Journal for Numerical Methods in Fluids</u>, 2010. (impact factor = 0.936)

Textbooks

- 21. **Dechaumphai, P.** and **Phongthanapanich, S.**, <u>Easy Finite Element Method</u> with Software, Alpha Science International, Oxford, 2009, 363 pages.
- 22. **Dechaumphai, P., Limtrakarn, W.**, Sujaritpawatskul, S. and Pratumwal, Y., Applications of Finite Element Method by SolidWorks Simulation, TPA Press, Bangkok, 2010, 572 pages.
- 23. **Dechaumphai**, P., Computational Fluid Dynamics By Finite Element and Finite Volume Methods, Second Edition, Chulalongkorn University Press, Bangkok, 2010, 677 pages.
- 24. **Dechaumphai, P.,** <u>Finite Element Method: Fundamentals and Applications,</u> Alpha Science International, Oxford, 2010, 572 pages.

<u>Patents</u>

- 25. **Suwantaroj, K.**, <u>The Yeast Pressing Machine for Mushroom</u>, Submitted on 13 October 2008, Requested Patent Number 0801005218.
- 26. Kaewkhiaw, P., Tiaple, Y. and **Juntasaro, V.**, <u>The New Design of the Marine Propeller to Reduce the Cavitation</u>, Submitted on 11 August 2010, Requested Patent Number 1001001225.

<u>รายชื่อนิสิตและนักศึกษาผู้สำเร็จการศึกษา</u>

1. นายปริญญา บุญมาเลิศ

2. นายสุธิ์ ไตรวิวัฒนา

นายอธิพงษ์ มาลาทิพย์

4. นายกีรติสุลักษณ์

5. นายเอกรงค์ สุขจิต

6. นายวัชพล โรจนรัตนางกูร

7. นายเกียรติศักดิ์ เหงื่ยมสูงเนิน

8. นายประชากร แก้วเขียว

9. นายอมรินทร์ ต้องกระโทก

10. นายชัชรินทร์ สิทธิ์ประเสริฐ

11. นายอนุวัฒน์ ยอดแสงคำ

12. นายบรรจง เคชาพานิชกุล

13. นายพรศิษย์ บุญมงคลรักษา

14. นายงสาวนโนชา นามเหลา

15. นายปพน พุทธธนาศักดิ์

16. นายวงศกร ภักดีพินิจ

17. นายปริญญา พงษ์ทอง

18. นายสุทธิคม พันธิมากรกิจ

19. นายพิชเญนทร์ โพธิคุณ

20. นาวสาวนิภาพร เติมแสงสิริศักดิ์

คุษฎีบัณฑิตวิศวกรรมเครื่องกล ดุษฎีบัณฑิตวิศวกรรมเครื่องกล ดุษฎีบัณฑิตวิศวกรรมเครื่องกล คุษฎีบัณฑิตวิศวกรรมเครื่องกล มหาบัณฑิตวิศวกรรมเครื่องกล มหาบัณฑิตวิศวกรรมเครื่องกล

รายชื่ออาจารย์นักวิจัยใหม่ผู้ได้เลื่อนสถานภาพทางวิชาการ

สถานะเมื่อเข้าร่วมโครงการ สถานะหลังจบโครงการ

1. ดร. วิโรจน์ ลิ่มตระการ ผู้ช่วยศาสตราจารย์ รองศาสตราจารย์

2. ดร. นิพนธ์ วรรณโสภาคย์ อาจารย์ ผู้ช่วยศาสตราจารย์